

CHAPTER 5

Excitation and Detection; Electrical Crosstalk

by: Albert Prak, MESA Research Institute, University of Twente, Enschede, the Netherlands

PART 1:

MODELING EXCITATION AND DETECTION MECHANISMS¹

5.I.1 Introduction

Many different mechanisms have been shown to be suitable for excitation and detection of mechanical structures. Brief, qualitative reviews over the available mechanisms have been presented in [5.1], [5.2], [5.3] and [5.4]. The aim of this chapter is to give a quantitative description of the mechanisms applied so far. The strategy is to describe all mechanisms in a similar way, such that they can be compared objectively. An important constraint that applies for all mechanisms is that the mechanical influence of the materials used for the transduction can be neglected. Since these materials in most cases have poorer mechanical properties than the base material of the resonator, our philosophy is that the active layers and metal electrodes should be very thin with respect to the base material. Excitation mechanisms to be discussed in this chapter are

- electrostatic excitation using an air gap
- electrostatic excitation using a thin dielectric film
- piezoelectric excitation
- magnetic excitation
- electrothermal excitation
- optothermal excitation.

Detection mechanisms to be discussed are

- electrostatic detection using an air gap

¹ Based on: A. Prak, *Silicon resonant sensors: Operation and response*, PhD-thesis, University of Twente, Enschede, the Netherlands, 1993.

- electrostatic detection using a thin dielectric film
- piezoelectric detection
- inductive detection
- piezoresistive detection
- optic methods such as interferometric, proximity and shutter detection.

The excitation mechanisms can be split up in two groups. The first one is based on reversible power exchange and energy storage. To this group belong the electrostatic, the piezoelectric and the magnetic excitation mechanisms. They are treated in section 5.I.2. The second group is based on energy dissipation (heating) and is irreversible as a consequence. It consists of the electrothermal and the optothermal mechanism. These mechanisms are described in section 5.I.3. D1F

Also two groups of detection mechanisms can be distinguished. The first group is actually the same as the first excitation group. Since the processes involved in these mechanisms are reversible, they can be used both for excitation and detection of the vibration. Hence they are treated in section 5.I.2. The other group (section 5.I.4) contains the piezoresistive and various optical mechanisms. They are based on irreversible mechanisms.

5.I.2 Reversible excitation and detection mechanisms

5.I.2.1 A simple example

Let us consider a simple system comprising a conducting movable plate hanged on a spring with a charge q , and a fixed plate, parallel to the first plate with a charge $-q$ (see fig. 5.1 and [5.6], section 8.2). The plate can move only in the y -direction. The system is characterized by two extensive variables: the position of the plate y and the charge q . The intensive variables are the force acting on the movable plate P and the voltage across the plates u . This system is a simple model for a resonator with one mode of vibration and one transducer for excitation/detection purposes. To be precisely, it concerns the electrostatic mechanism using an air gap, see next subsection. It is also a simple model for a condenser microphone and for a capacitive pressure sensor. This system has two energy ports: an electrical (q, u) and a mechanical (y, P).

We will use the energy method (a physical system approach) to model the system (see e.g.

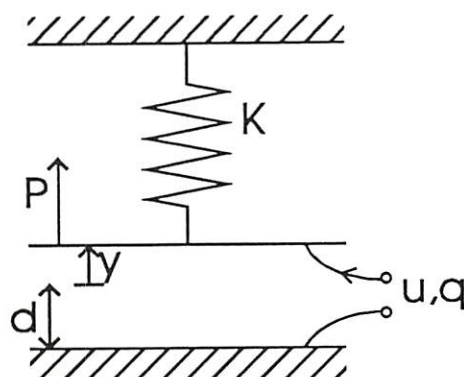


Fig. 5.1: Simple model for the electrostatic mechanism using an air gap. This model also applies for a condenser microphone or a capacitive pressure sensor.

Grid legge

[5.5], [5.6]). The first step of this method is to express the total energy of the system in the extensive variables (in this case y and q). The energy consists of a mechanical part and an electrical part. Starting from the initial state ($y = 0, q = 0$), the energy can be found by subsequently moving the plate to a position y_0 , and charging the capacity with a charge q_0 . The result is:

$$E(y, q) = \frac{1}{2} K(y + d)^2 + \frac{1}{2} \frac{q^2}{C(y)}$$

with d the spacing between the plates at the initial state, and $C(y)$ the capacitance:

$$C(y) = \epsilon_0 \frac{A}{d + y}$$

where A is the surface of the plates. The force and voltage can be found as follows:

$$P = \left(\frac{\partial E}{\partial y} \right)_q = Ky + \frac{1}{2} \frac{q^2}{\epsilon_0 A} \quad ; \quad u = \left(\frac{\partial E}{\partial q} \right)_y = \frac{q(d+y)}{\epsilon_0 A}$$

For excitation and detection of vibrations in this device, we are interested in small variations (denoted by dy , dP , dq and du , respectively) around an equilibrium (static) bias setting (denoted by y_0 , P_0 , q_0 and u_0):

$$dP = \left(\frac{dP}{dy} \right)_{q=q_0} dy + \left(\frac{dP}{dq} \right)_{y=y_0} dq = Kdy + \frac{q_0}{\epsilon_0 A} dq$$

$$du = \left(\frac{du}{dy} \right)_{q=q_0} dy + \left(\frac{du}{dq} \right)_{y=y_0} dq = \frac{q}{\epsilon_0 A} dy + \frac{d+y_0}{\epsilon_0 A} dq$$

If the small variations are harmonic (sinusoidal) we can write:

$$\begin{vmatrix} \bar{u} \\ \bar{P} \end{vmatrix} = \frac{1}{j\omega} \begin{vmatrix} (d+y_0)/\epsilon_0 A & q_0/\epsilon_0 A \\ q_0/\epsilon_0 A & K \end{vmatrix} \begin{vmatrix} \bar{q} \\ \bar{y} \end{vmatrix} = \frac{1}{j\omega} \begin{vmatrix} c_{11} & c_{12} \\ c_{21} & c_{22} \end{vmatrix} \begin{vmatrix} \bar{q} \\ \bar{y} \end{vmatrix}$$

where the overstrike indicates the amplitude of the harmonic variation, and ω is its angular frequency. The above matrix equation is called the constituent equation of the transducer.

The off-diagonal matrix elements (c_{12} and c_{21}) couple the electrical variables to the mechanical variables: electromechanical transduction is only possible if these matrix elements are non-zero. We immediately see that the transducer will not work if it is not biased with a charge q_0 . (Note: instead of a bias charge q_0 , a bias voltage u_0 can be used. This bias voltage can be entered in the matrix using the equation $C(y_0) = u_0/q_0$).

applications

The electrostatic transduction mechanism is reversible, which means that with the same transducer, electrical energy can be converted to mechanical energy (this corresponds to excitation of the resonator) and mechanical energy can be converted to electrical energy (this corresponds to detection of the resonator).

In the first case, we can for example control the resonator with an AC voltage $\bar{u}=1$ V. In order to calculate the amplitude of the coordinate y , we need to know how the system is mechanically loaded. The mechanical load consists of a mass M and friction coefficient R (Note: the mass can also be included in the energy function, but in the above we have not regarded the mass as a part of the system; therefore we have to regard it here as a load to the system). The deflection can now be found from the following set of equations:

$$\begin{cases} \bar{u} = 1 \\ \bar{P} = -j\omega M\bar{y} - R\bar{y} \\ \left| \begin{matrix} \bar{u} \\ \bar{P} \end{matrix} \right| = \frac{1}{j\omega} \begin{vmatrix} c_{11} & c_{12} \\ c_{21} & c_{22} \end{vmatrix} \begin{pmatrix} \bar{q} \\ \bar{y} \end{pmatrix} \end{cases}$$

The first two equations are called phenomenological equations: they tell us how the system is connected to the outside world (how the energy ports are loaded / controlled). The result is:

$$\bar{y} = \frac{\bar{u}q_0 / (d + y_0)}{K - \omega^2 M + Rj\omega - \frac{q_0^2}{\epsilon_0 A(d + y_0)}}$$

Remember that instead of a bias charge q_0 a bias voltage u_0 can be used. The denominator shows a clear second order (resonance) characteristic, the standard form of which is:

$$\frac{1}{1 - \frac{\omega^2}{\omega_0^2} + \frac{j\omega}{Q\omega_0}}$$

where ω_0 is the resonance frequency and Q the quality factor. The resonance frequency of the biased resonator deviates from the resonance frequency based on pure mechanical considerations (the effective spring constant deviates by an amount $(q_0^2(d+y_0)) / (\epsilon_0 A)$). This deviation depends on the bias charge/voltage. Note that we have used here a voltage to address the resonator. In case of a current controlled resonator, we would find that the resonance frequency does not depend on the bias signal, and equals the mechanical resonance frequency $(K/M)^{1/2}$.

If the transducer is used to detect vibrations (of amplitude \bar{y}) we obtain from the equations:

$$\bar{u} / \bar{q} = -R$$

$$\begin{vmatrix} u \\ P \end{vmatrix} = \frac{1}{j\omega} \begin{vmatrix} c_{11} & c_{12} \\ c_{21} & c_{22} \end{vmatrix} \begin{vmatrix} \bar{q} \\ \bar{y} \end{vmatrix} \quad (R \text{ is the load resistance at the electrical terminal})$$

the result:

$$\bar{u} = \bar{y} \frac{c_{12}}{1 + c_{11}/j\omega R}$$

Most important conclusion is that the phase of the measured electric signal depends strongly on the value of the load impedance.

5.I.2.2. Extension to more complicated systems

In case we use a continuous system (like the clamped-clamped beam) as the resonator the above procedure is still applicable. However, a few modifications have to be made:

- Mechanically, the structure is distributed, which means that it possesses an infinite number of degrees of freedom. Consequently, in contrast to the previous simple resonator, we need an infinite number of coordinates to describe the system. It is very useful to take the modal coordinates, which were introduced in the chapter 3, as the coordinates of the system. In practice it is not necessary to deal with an infinite number of modes: accurate simulations can be obtained with only a few modes. The modal coordinates are the system's mechanical extensive variables. The corresponding intensive variables are the modal forces, which were also introduced in chapter 3.

- In practice, the resonator can be supplied with multiple transducers, e.g. one for excitation and one for detection of the vibration. In the previous simple case, there was only one such (electrostatic) transducer. The power flow of every electromechanical transducer is characterized by an intensive variable (in the electrostatic case the voltage u) and an extensive variable (a charge q).

If the n modes of vibration are taken into account, and the resonator has m transducers for excitation/detection, there are $n+m$ energy ports (see fig. 5.2). The constituent equation is an $n+m$ by $n+m$ matrix:

$$\begin{matrix} \bar{u}_1 & | & E_{1,1} & \dots & E_{1,m} & C_{1,1} & \dots & C_{1,n} & | & \bar{q}_1 \\ \vdots & | & \ddots & \vdots & \vdots & \ddots & \vdots & \vdots & | & \vdots \\ \bar{u}_m & | & E_{m,1} & \dots & E_{m,m} & C_{m,1} & \dots & C_{m,n} & | & \bar{q}_m \\ \bar{P}_1 & = & C_{1,1}^T & \dots & C_{1,m}^T & M_{1,1} & \dots & M_{1,n} & | & \bar{y}_1 \\ \vdots & | & \ddots & \vdots & \vdots & \ddots & \vdots & \vdots & | & \vdots \\ \bar{P}_n & | & C_{n,1}^T & \dots & C_{n,m}^T & M_{n,1} & \dots & M_{n,n} & | & \bar{y}_n \end{matrix} \quad (5.1)$$

with:

↑
extensive
variables

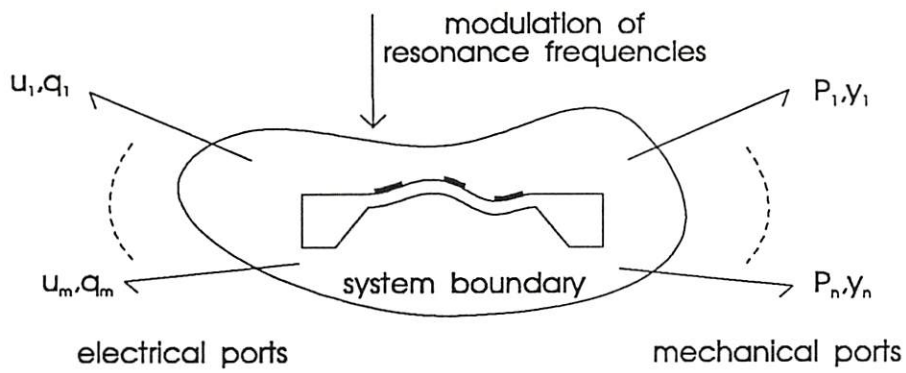


Fig. 5.2: Visualization of the model for reversible mechanisms. The system comprises n modes of vibration and m transducers for excitation detection purposes.

$$E_{ij} = \frac{1}{j\omega} \left(\frac{\partial^2 E}{\partial q_i \partial q_j} \right)_0 ; \quad M_{ij} = \frac{1}{j\omega} \left(\frac{\partial^2 M}{\partial y_i \partial y_j} \right)_0 ; \quad C_{ij} = \frac{1}{j\omega} \left(\frac{\partial^2 C}{\partial q_i \partial y_j} \right)_0 \quad (5.2.a;b;c)$$

Eq. (5.1) is often referred to as the constituent equation of the system. The right column represents the amplitudes of the time derivatives of the extensive variables, also called extensity flows or just flows. In the electrostatic and piezoelectric mechanisms, these are the currents, and in the magnetic mechanism the voltages. The total matrix is composed of four submatrices: a matrix E coupling the electrical variables to each other, a matrix M coupling the mechanical variables to each other, and a matrix C coupling the electrical variables to the mechanical variables. Due to the Maxwell symmetry, the matrix C^T is the transposed matrix of the C-matrix, and the E and M-matrices are symmetrical. The fact that the C-matrix contains elements which are different from zero is a necessary condition for the conversion from electrical energy into mechanical energy and vice versa. Off-diagonal elements of the E-matrix represent direct coupling between the electrical ports (electrical cross-talk), and off-diagonal elements of the M-matrix represent direct coupling between the modes.

5.I.2.3 Electrostatic excitation and detection using an air gap

The configuration for electrostatic excitation by means of an air-gap capacitor is sketched in fig. 5.3. The 'excitation version' of the mechanism works by means of Coulomb forces between the capacitor plates. In the detection mode, the change in the capacitance due to the motion of the structure is measured. The mechanism is commonly applied in micromechanical resonant sensors. In some devices, the mechanism is used for both excitation and detection. Both configurations with separate transducers for excitation and detection (e.g. [5.7], [5.8], [5.9] and [5.10]) as well as configurations using the same transducer for excitation and detection (e.g. [5.11]) are reported. Also devices with electrostatic excitation using other detection mechanisms, e.g. piezoresistive detection (see [5.12], [5.13] and [5.14]) are very common.

We will not follow the whole route from deriving the energy function to the constituent equation. We suffice with some intermediate results. For the system's energy holds:

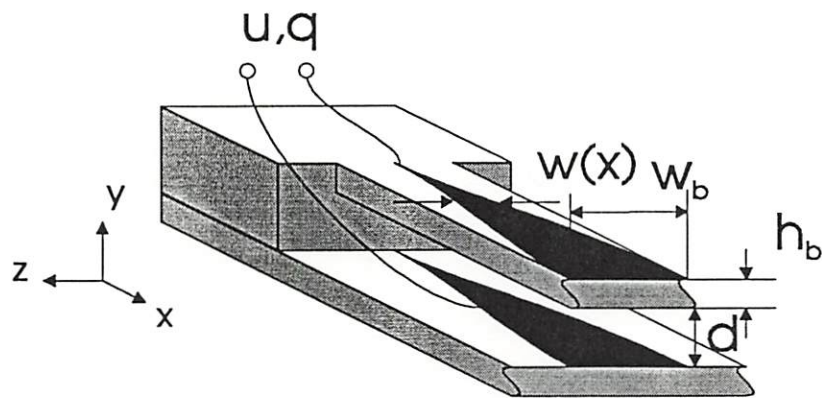


Fig. 5.3: Configuration of the electrostatic mechanism using an air gap.

$$E = \frac{1}{2} \sum_{j=1}^{\infty} K_j y_j^2 + \frac{1}{2} \sum_{i=1}^m \frac{q_i^2}{C_i} \quad (5.3)$$

where q_i is the charge on one plate of the i -th capacitor and C_i the capacitance of the i -th capacitor, for which we assume:

$$C_i(y_1, \dots, y_n) = \int_0^l \frac{\epsilon_0 w_i(x)}{d + \sum_{j=1}^n y_j v_j(x)} dx \quad (5.4)$$

with w_i the x -dependent electrode width, d the gap spacing at zero deflection and ϵ_0 the permittivity of free space. The numerator in eq. (5.4) equals the actual gap spacing, which is $d+v(x)$, where $v(x)$ was expanded in the mode shapes (see chapter 3).

The constituent equation of this system with $n+m$ ports can be found by scrupulously following the procedure sketched in section 5.I.2.1. To be terse, we will consider only one mode and one electric terminal. The simple device obtained in this way is very illustrative for a more general case. In great extent, it can be compared to the example device in section 5.I.2.1. However, this time the movable capacitor plate is curved in a shape resembling the mode shape, resulting in more complex matrix coefficients. With eqs. (5.2) and (5.3) we find:

$$\left| \begin{array}{c} \bar{u}_1 \\ \bar{P}_1 \end{array} \right| = \frac{1}{j\omega} \left| \begin{array}{cc} \frac{1}{C_{1,0}} & -\frac{q_{1,0}}{C_{1,0}^2} \frac{\partial C_{1,0}}{\partial y_1} \\ -\frac{q_{1,0}}{C_{1,0}} \frac{\partial C_{1,0}}{\partial y_1} & K_1 - \frac{q_{1,0}^2}{2C_{1,0}^2} \left[\frac{\partial^2 C_{1,0}}{\partial y_1^2} - \frac{2}{C_{1,0}} \left(\frac{\partial C_{1,0}}{\partial y_1} \right)^2 \right] \end{array} \right| \left| \begin{array}{c} \bar{q}_1 \\ \bar{y}_1 \end{array} \right| \quad (5.5)$$

A subscript '0' refers to the value of the quantities at the bias set-point.

5.I.2.4 Electrostatic excitation and detection using a thin dielectric film

This mechanism is not very commonly used, probably because of its relative low efficiency. However, in our opinion it certainly has potential applications because of its technological ease. The mechanism was first demonstrated in [5.15]. Later on, the mechanism has been applied in [5.16] and [5.17]. The configuration of the mechanism is shown in fig. 5.4. It consists of a dielectric film sandwiched between two electrodes, the mechanical effect of which is neglected here. This three layer structure is deposited on a relatively thick silicon structure that has to be excited, or whose vibration has to be measured. The physical operation of the mechanism is discussed at the end of this section.

The energy function of the system is the same as that for the electrostatic mechanisms using an air gap, eq. (5.3). However the expression for the capacitance is different:

$$C_i = \int_0^l \frac{\epsilon_{22} w_i(x) (1 + S_1(x))}{h(1 + S_2(x))} dx \quad (5.6)$$

where ϵ_{22} denotes the dielectric constant of the film in the y -direction, $S_1(x)$ the strain in the x -direction and $S_2(x)$ the strain in the y -direction of the film. We have derived the constituent equation for a device with one mode of vibration, and one electromechanical transducer (assuming the film is much thinner than the beam):

$$\left| \begin{array}{c} \bar{u}_1 \\ \bar{P}_1 \end{array} \right| = \frac{1}{j\omega} \begin{vmatrix} \frac{h_1}{\epsilon_{22} A_1} & u_{1,0} \frac{h_b}{2} \frac{1}{1-\nu_1} \frac{W_{11}}{A_1} \\ u_{1,0} \frac{h_b}{2} \frac{1}{1-\nu_1} \frac{W_{11}}{A_1} & K_j - u_{1,0}^2 \epsilon_{22} \frac{h_b^2}{4h_1} \frac{1}{(1-\nu_1)^2} \left(\nu_1 W_{111}^* - \frac{W_{11}^2}{A_1} \right) \end{vmatrix} \begin{array}{c} \bar{q}_1 \\ \bar{j}_1 \end{array} \quad (5.7)$$

The variable $u_{1,0}$ denotes the bias voltage, h_b the thickness of the beam, h_1 the thickness of the thin film and ν_1 Poisson's ratio of the thin film. A_i and W_{ijk}^* are defined as:

$$A_i = \int_0^l w_i(x) dx \quad (5.8)$$

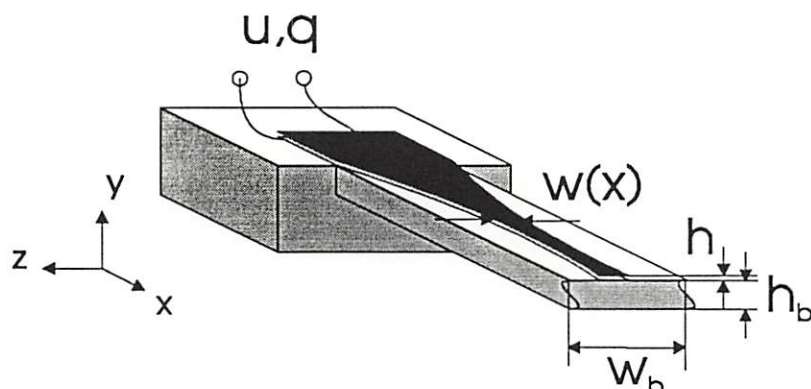


Fig. 5.4: Configuration of the electrostatic (thin film) and the piezoelectric mechanism.

$$W_{ijk}^* = \int_0^l w_i(x) v_j''(x) v_k''(x) dx \quad (5.9)$$

A_i denotes the area of the electrode of the i -th electric terminal. The W_{111} term in eq. (5.7) affects the mechanical spring constant (due to the elongation of the film, the stiffness of the structure changes somewhat when a voltage is applied). Further,

$$W_{ij} = \int_0^l w_i(x) v_j''(x) dx \quad (5.10)$$

is related to the relative surface change of the i -th electrode due to bending in mode j .

Remarkable is that the mechanism also works if $v_1=0$, since it was long believed that the operating principle is that the applied voltage causes a squeezing of the film, which via Poisson's ratio causes an elongation, and thus a bending of the beam. However, the film will also elongate when $v_1=0$, since charges on the electrode tend to expand the film. Thus actually two mechanisms work simultaneously.

5.I.2.5 Piezoelectric excitation and detection

A piezoelectrically operated resonator (see e.g. [5.18] and [5.19]) consists of a piezoelectric film, sandwiched between two electrodes. The three layer structure is deposited on a structure in which the vibration has to be activated or detected (see fig. 5.4, the figure for electrostatic excitation and detection using a thin dielectric film).

Calculating the energy function is a rather extensive procedure, which we will not reproduce here. The 'intrinsic' constituent equation of the piezoelectric film material plays an important role in deriving the constituent equation of the whole device. This intrinsic constituent equation reads:

$$\begin{vmatrix} S_1 \\ D_2 \end{vmatrix} = \begin{vmatrix} s_{11}^* & d_{31}^* \\ d_{31}^* & \varepsilon_{33}^* \end{vmatrix} \begin{vmatrix} T_1 \\ E_2 \end{vmatrix} \quad (5.11)$$

In this equation, S_1 and T_1 denote the strain and stress in the x -direction, and D_2 and E_2 the dielectric displacement and field strength in the y -direction respectively. Further, s_{11} , d_{31} and ε_{33} are the compliance (at constant field strength), piezoelectric coefficient and permittivity (at constant stress) respectively. The meaning of the asterisk will be explained below. Eq. (5.11) can be obtained from the general 9x9 tensor equation (see e.g. [5.20]) of piezoelectric materials under the following assumptions: no electric fields in the x and z -direction, no shear stresses, no stress in the y -direction and no strain in the z -direction (plate-like bending). Further it is assumed that the piezoelectric material has a hexagonal symmetry with respect to the c -axis (class 6mm [5.20], e.g. ZnO). Under the assumptions stated above, it can be shown that $s_{11}^* = s_{11}(1-\nu^2)$, $d_{31}^* = d_{31}(1+\nu)$, and $\varepsilon_{33}^* = \varepsilon_{33}(1-k_{31}^2)$, where $k_{31}^2 = d_{31}^2/s_{11}\varepsilon_{33}$ is an intrinsic coupling factor and $\nu = -s_{12}/s_{11}$ is a Poisson's ratio.

The constituent equation for a device with one electric terminal and taking only one mode into account reads:

$$\left| \begin{array}{c} \bar{u}_1 \\ \bar{P}_1 \end{array} \right| = \frac{1}{j\omega} \left| \begin{array}{cc} \frac{h_1}{\varepsilon_{33}^* A_1 (1 - k_{31}^{*2})} & \frac{1}{2} \frac{h_b h_1}{A_1} \frac{1}{d_{31}^*} \frac{k_{31}^{*2}}{1 - k_{31}^{*2}} W_{11} \\ \frac{1}{2} \frac{h_b h_1}{A_1} \frac{1}{d_{31}^*} \frac{k_{31}^{*2}}{1 - k_{31}^{*2}} W_{11} & K_j + \frac{h_b^2 h_1}{4 A_1 s_{11}^*} \frac{1}{1 - k_{31}^{*2}} W_{11}^2 \end{array} \right| \left| \begin{array}{c} \bar{q}_1 \\ \bar{y}_1 \end{array} \right| \quad (5.12)$$

The constituent equations of piezoelectric bimorphs have also been derived by Smits et al. [5.21] and [5.22]. Their study is more general in the sense that the film needs not to have a negligible thickness: its influence is accounted for. However, the mechanical load is confined to a concentrated force or moment at the tip, or a uniform pressure on the entire cantilever beam.

5.I.2.6 Magnetic excitation and detection

A number of configurations is possible for a magnetic operation of a resonant structure. In this section, the configuration is discussed in which an (alternating) current is led along the resonant beam which is placed in a homogeneous, permanent magnetic field (fig. 5.5). The mechanism has been successfully realized, and is applied in a few micromechanical devices, e.g. [5.23]. The excitation is effected by Lorentz forces acting upon the current conducting resonator. The detection signal is caused by the flux changes in the current loop due to the motion of the beam (i.e. the change of the area of the loop). The flux change due to the change in the coefficient of self-inductance is neglected. The transduction is between the mechanical and the magnetic domain instead of the electric domain as in the previous mechanisms. The consequence of this is that the coupled flux ϕ^c is the extensive variable, and its time derivative (the voltage) is the flow. The current i is the intensive-variable. For a system with one magnetic port and one mode, the following constituent equation can be derived:

$$\left| \begin{array}{c} \bar{i} \\ \bar{P}_j \end{array} \right| = \frac{1}{j\omega} \left| \begin{array}{cc} \frac{1}{L} & -\frac{B}{L} V_j \\ -\frac{B}{L} V_j & K_j + \frac{B^2}{L} V_j^2 \end{array} \right| \left| \begin{array}{c} \bar{\phi}^c \\ \bar{y}_j \end{array} \right| \quad (5.13)$$

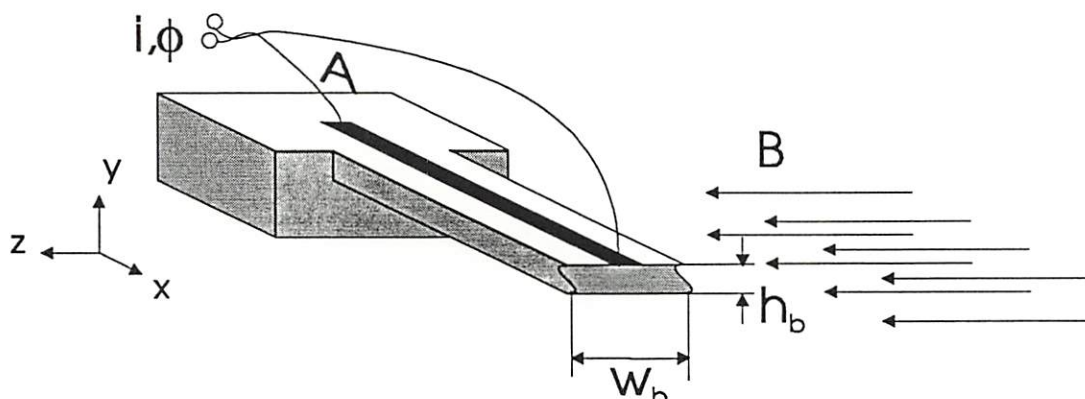


Fig. 5.5: Configuration of the magnetic mechanism.

where $V_j = \int_0^l v_j(x) dx$ is the change of the loop's projected surface per unit modal deflection, B

the magnetic field strength and L the coefficient of self inductance of the current loop.

5.I.3 Irreversible excitation mechanisms

This section describes the excitation of microstructures by thermal expansion. Just thermal expansion is not an irreversible effect. The reason why the mechanisms are classified as irreversible is that the heat is generated by an irreversible mechanism, namely by ohmic heating or by photon-absorption. This means that in contrast to the mechanisms described in the previous section, these mechanisms can not be applied in a detection mode. A complete description with the energy method is not possible. However, a modal excitation force can still be computed. This will be the purpose of this section.

The principle of the mechanism is that heat, obtained either from the electric or the radiant domain, is applied at the top side of the resonator. The heat generated at the surface will diffuse into the y -direction, and hence a gradient in the temperature will be created. Due to thermal expansion of the material a mechanical moment, resulting in a bending of the resonator will be induced.

The model presented here is based on the work of Lammerink et al., an overview of which is given in [5.16]. In their work, expressions for the thermally induced mechanical moments are derived. These can be converted to the modal forces. Another model concerning optothermal excitation of microstructures is described in [5.24].

In [5.16], the problem is approached by first solving the temperature distribution in the beam, for which a one-dimensional diffusion model is used. The one-dimensional approach is not valid in the low frequency regime, where thermal diffusion lengths are generally large. The thermally induced mechanical moment can be calculated from the temperature distribution.

5.3.1 Electrothermal excitation

In this mechanism, all heat is supposed to be injected at the upper surface of the beam by a resistive pattern on top of the structure, see fig. 5.6. The mechanism is applied in a number of devices [5.25], [5.26], [5.27], [5.28] and [5.29]. In the model presented in [5.16], the heat is assumed to be injected homogeneously over a certain fraction of the length of the resonator, and the calculated moments are the concentrated moments, generated at the edges of the homogeneously heated area. However, in this thesis we prefer to work with an x -dependent heat-source, such that the possibility of arbitrarily shaped resistive patterns is left open. The injected power per unit length equals: $p(x) = i^2 r / (h w(x))$, where r is the resistivity of the film material, i is the current and h and $w(x)$ are the thickness and width of the film respectively. The dissipated power per unit length consists of a static and a dynamic component. The static component has no direct effect on the dynamic behaviour. It modulates the temperature dependent parameters such as Young's modulus, the density, the dimensions and the thermal properties.

$$T_0 \rightarrow E(T), \rho(T), \epsilon(T), \alpha(T)$$

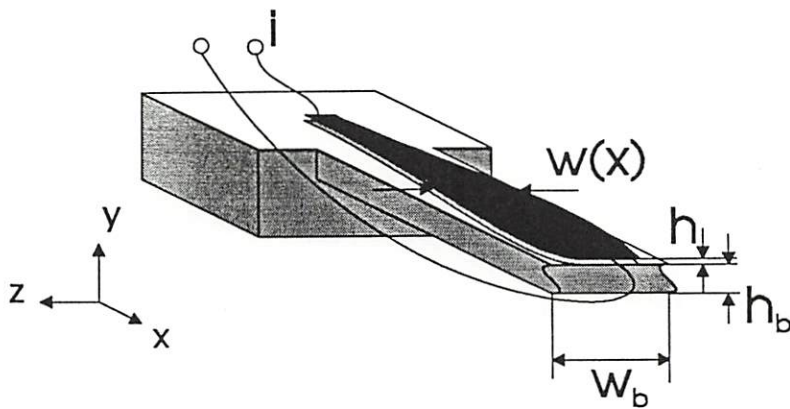


Fig. 5.6: Configuration of electrothermal excitation and piezoresistive detection.

The following expression for the excitation load can be obtained:

$$P_e(x) = -p''(x) \frac{12E_b I}{w_b k_t} \alpha \Gamma_1(\gamma) \quad (5.14)$$

where k_t and α are the heat conductivity and coefficient of thermal expansion of the material respectively and I is the moment of inertia of the beam. The function Γ_1 is defined as:

$$\Gamma_1(\gamma) = \frac{1}{\gamma^2} \left(\frac{1}{2} + \frac{1}{\gamma} + \frac{2}{\gamma(1+e^{-\gamma})} \right) \quad (5.15)$$

with γ a dimensionless, frequency dependent, complex number which can be identified as the normalized wavenumber of the thermal waves.

4.3.2 Optothermal excitation

In this mechanism, heat is applied by an optical or infrared source which irradiates the top of the structure. The mechanism (see fig. 5.7) is often used in combination with optic detection techniques to obtain all-optic devices which are immune to electromagnetic fields, and available for use in harsh environments. Devices with optothermal excitation are described in [5.30], [5.24], [5.31], [5.32] and [5.33]. The major difference with electrothermal excitation is that the light penetrates the structure, such that the heat-source is not located at top of the structure any longer. For simplicity, the thermal and optical properties will be assumed uniform over the entire structure. However, the absorbed power per unit length is allowed to depend on x . This can be achieved by illuminating the structure inhomogeneously, or by depositing a film of variable width with an absorption coefficient different from the beam material. In the last case, the absorbed power per unit length equals: $p(x) = I_0(w(x)(R_b - R_f) + w_b(1 - R_b))$, where R_b and R_f are the coefficients of reflection of beam and film respectively, and I_0 is the intensity of the light. The modal forces turn out to be [5.16]:

$$P_j = K_j y_j - \frac{12E_b I \alpha}{w_b k_t} \Gamma_2(\gamma, \xi) \int_0^l p''(x) v_j(x) dx \quad (5.16)$$

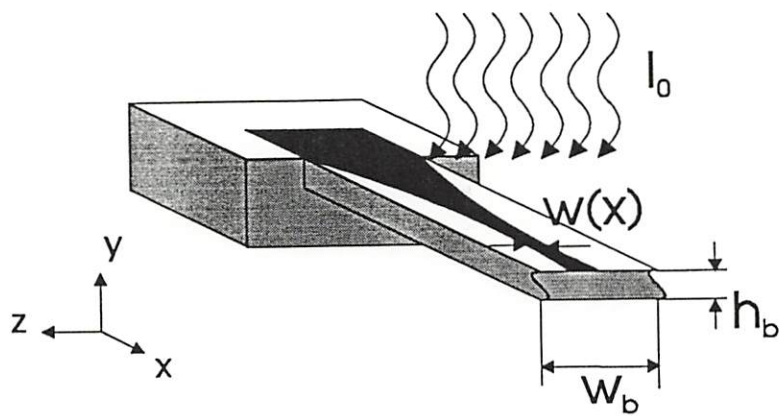


Fig. 5.7: Configuration of optothermal excitation.

where the function $\Gamma_2(\gamma, \xi)$ is similar to the function $\Gamma_1(\gamma)$, with the only difference that it also depends on the normalized penetration depth ξ of the light. For relative short penetration depths, Γ_2 does not depend on ξ , while for a relatively long penetration depth, the modulus of Γ_2 decays with ξ^2 . The γ dependence of Γ_2 is the same as Γ_1 . For further details concerning the opto-thermal excitation we refer to [5.16].

If bare semiconductor materials are irradiated, photo-electronic strain effects can occur. The effect manifests itself by a deviant phase-frequency relation as compared to pure thermally excited beams. A theoretical model and experimental results on the influence of the electronic strain are described in [5.34].

5.I.4 Modulator-type detection mechanisms

In this class of mechanisms, the vibration is detected by means of an energy-flow which is generated by an auxiliary source. The energy flow of this source is modulated by the vibration. In a first order approximation, there is no energetic coupling between the energy flow from the auxiliary source and any energy port of the transducer. This makes a description by the energy method impossible. Examples of modulator-type detection mechanisms being used in existing devices are the piezoresistive detection where the resistance of the detecting resistor (and hence the current/voltage across it) is modulated by a deformation of the resistor, and optical detection techniques such as interferometric detection, shutter detection and the beam deflection method.

5.I.4.1 Piezoresistive detection

Piezoresistive materials show a change of the resistivity under application of a mechanical strain. Besides, the resistance of a certain pattern will change due to dimensional changes. The change in resistance is characterized by the gauge factor G , which is defined as the relative change of the resistance of the pattern per unit strain. For homogeneous materials with isotropic elastic properties, the gauge factor equals [5.35]:

$$G = 1 + 2\nu + \frac{\Delta r}{rS} \quad (5.17)$$

where ν is Poisson's ratio, S the strain, r the resistivity and Δr the change of the resistivity. The first two terms are due to the dimensional change, and the latter due to the change in resistivity. Silicon (mono- as well as polycrystalline) is an excellent piezoresistive material with gauge factors varying from 10 to 100. For large gauge factors ($G \gg 1$) the intrinsic effect is dominant, and the dimensional effect can be neglected. In that case, we find:

$$\bar{R} = Gr_0 \frac{h_b}{2h} \int_0^l \frac{\bar{v}''(x)}{w(x)} dx \quad (5.18)$$

with r_0 the resistivity at zero deflection, and \bar{R} the harmonic variation of the resistance. The resistivity changes can be measured using a current or voltage-source. As an example, the harmonic part of the voltage is given due to a current i_0 :

$$\bar{u} = i_0 Gr_0 \frac{h_b}{2h} \int_0^l \frac{\sum_i \bar{y}_i v_i''(x)}{w(x)} dx \quad (5.19)$$

where eq. (3.17.a) has been used.

5.I.4.2 Optical detection techniques

For characterization of devices, very often non-miniaturized, bulk optical interferometer set-ups are used [5.17] and [5.36]. In a commercial sensor this is not an interesting alternative. However, several fiber optical methods have been shown to be suitable as a detection technique. A quantitative treatment of these techniques is beyond the scope of this course, since an immense number of (often uncontrollable) parameters such as reflection coefficients, surface roughness, angular misalignment, transverse offset, wavelength, intensity, numerical aperture of the fibers (to mention a few), are involved. Therefore, the mechanisms will be discussed in a qualitative way, and very briefly. The sensitivity depends on lots of factors, but is typically in the (sub)nanometer range. The following mechanisms have been described in the literature:

- Single mode fiber optical interferometer method [5.37], see fig. 5.8.a. Two fibers are fused along a certain distance in the middle to form an X-junction. From the four terminals, one is used for coupling in the light, one to measure the out coming light, and one is placed in front of the surface the deflection of which has to be measured. One terminal is not used and ends in a matching fluid. Two interfering signals are set up at the terminal near the vibrating structure, namely the wave reflected directly from the end of the fiber, and the wave coupled back into the fiber after reflection from the vibrating structure.

- Fabry-Perot interferometer method [5.38], see fig. 5.8.b. In contrast to the previous method, a cavity is situated entirely in the micromachined device. It is composed of two mirrors, one of which has to be semi-transparent in order to let the light in and out. One mirror is formed by the vibrating structure. In [5.38], it is demonstrated how this set-up can be used to make a self-oscillator.

- Optical beam deflection method [5.39], see fig. 5.8.c. The light coming from a fiber is, after reflection on the vibrating structure coupled into the same or another fiber. The angular rotation of the vibrating structure modulates the amount of light coupled in the second fiber. The method is also applied in a bulk-optical version. In this case, the same signal-to-noise ratio as in a bulk optical Michelson interferometer can be obtained [5.40].

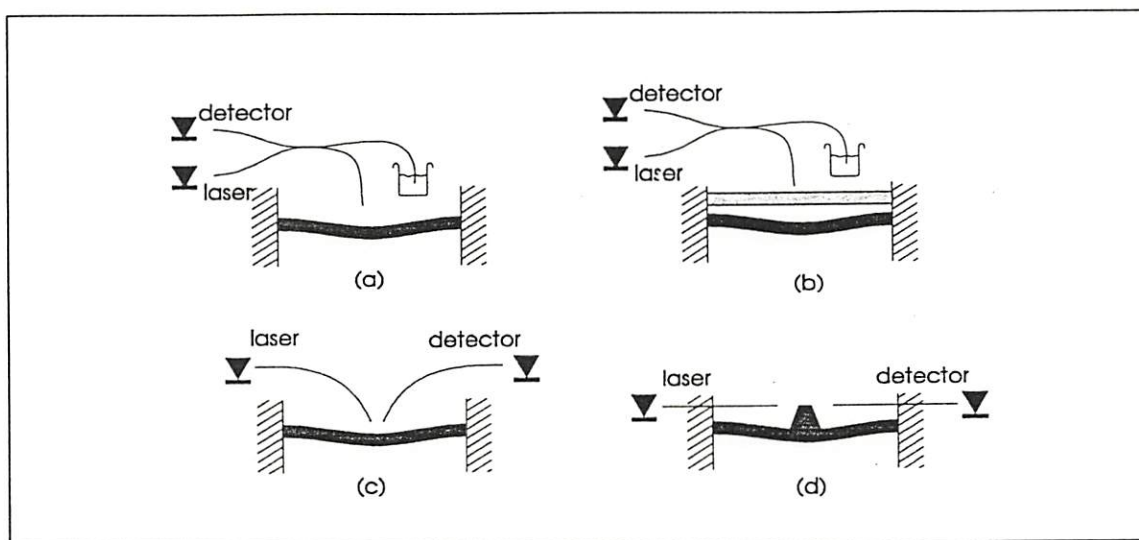


Fig. 5.8: Various optical detection schemes. (a) fiber optic detection method, (b) Fabry-Perot interferometer method, (c) beam deflection method and (d) shutter method.

- Shutter method [5.39], see fig. 5.8.d. A light ray coming from a fiber is partly held by a boss on the resonating structure after which it is coupled into another fiber. The intensity of the transmitted light is a measure for the position of the resonator. In the case of [5.39], this technique appeared to be a hundred times more sensitive than the optical beam deflection method.

Of course, other alternatives will be possible.

PART II:

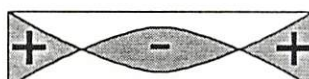
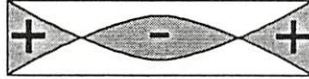
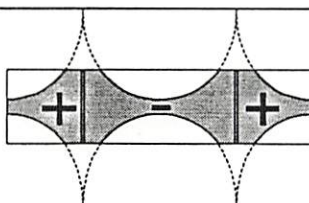
A COMPARATIVE REVIEW

5.II.1 Selective mode excitation and detection

A method was presented which allows a full control over the strength and sensitivity with which the individual modes of vibration are excited and detected [5.41]. The basic idea of the method is to shape the electrodes (or light absorbing layers) on the resonator in a shape reminiscent of the mode shapes. The method is applicable to most excitation and detection mechanisms described in the previous chapter. An overview of the design rules of the electrode shapes necessary to excite and detect specific modes is given in table 5.1. Mechanisms for which the method is hard to realize are:

- Magnetic excitation/detection: In this case, refined control over the spatial distribution of the B -field must be obtained. When the field is created by bulk permanent or electro-magnets, this task is very difficult. A solution might be to create a permanent local B -field in the environment of the resonator by deposition of magnetic materials like CoCr. By properly shaping this film, the correct field for excitation and detection of specific modes might be

Table 5.1: Shapes of the transducers for selective excitation and detection of the first mode of a microbridge (w is the width of the transducer, v_1 is the first mode shape)

mechanism	shape of transducer	top view of transducer
electrostatic excitation (air gap) electrostatic detection (air gap)	$w(x) \propto v_1(x)$	
piezoelectric excitation electrostatic excitation (thin film) optothermal excitation	$w(x) \propto \int \int v_1(x) dx dx + c_1 x + c_2$ $c_1 = 0 ; c_2 = 0$	 $c_1 = 0 ; c_2 \neq 0$
electrothermal excitation	$w(x) \propto \frac{1}{\int \int v_1(x) dx dx + c_1 x + c_2}$ $c_1 = 0 ; c_2 \neq 0$	
piezoelectric detection electrostatic detection (thin film)	$w(x) \propto \frac{d^2 v_1(x)}{dx^2}$	
piezoresistive detection	$w(x) \propto 1 / \frac{d^2 v_1(x)}{dx^2}$	

obtained.

- All optical detection techniques: However, devices can be designed such that the detected signal is proportional to the spatial integral over the product of the light distribution function and the amplitude of the vibrating structure. The fact that the first mode shape of a microbridge shows likeness to a Gaussian function can be exploited to detect this mode selectively.

An important consequence of not being able to suppress undesired modes is that tighter requirements must be made with respect to the peripheral electronics, since in that case unwanted modes must be filtered out electronically.

5.II.2 Magnitude and scaling laws of the excitation forces

The magnitude of the forces that can be generated is an important criterion for the quality of the excitation mechanisms. In this section the motion of the beam is supposed to be suppressed by some external fixture ($y_f=0$) and the force which the fixture has to exert on the resonator to keep it at $y_f=0$ will be calculated. This is believed to be a good indication for the strength of the mechanism.

A situation with one mode and one transducer element will be considered, thereby assuming a shape of the transducer element which only excites the first mode of vibration (for how to achieve this see [5.41]). The maximum width of the transducer element is put equal to w_{max} . The resulting shapes are listed in the second column of table 5.2. In the electrostatic mechanism with a thin film, the piezoelectric mechanism, and the optothermal mechanism the integration constants, which can be chosen arbitrary in designing the shape, have been chosen such that the minimum film width equals zero. In the latter mechanism the reflection coefficients of beam and film have been taken 1 and 0 respectively. In the electrothermal mechanism, the integration constant $C_1 > 0.0543$. When $C_1 = 0.0543$, the minimum film width equals zero, and the resistance of the film will be infinite.

In view of miniaturization of the devices it is important to deal with the effect of geometrical scaling. A distinction could be made between scaling of the device dimensions and scaling of the dimensions related to the transducers. In this section, we discuss proportional scaling of the device as a whole. The scaling factor, defined by the exponent x in $P_1 \propto Dim^x$, where Dim represents a linear dimension of the device, is given in the last column of table 5.2. Since it would not be realistic to look only at the effect of geometrical scaling, more than one scaling factor is given for most mechanisms. In many cases, driving voltages and currents cannot be kept constant when miniaturizing the structure. In the electrostatic mechanism with an air gap for example, it is realistic to keep the bias voltage at a constant proportion to the pull-in voltage (the voltage at which the beam collapses on the ground electrode). In the electrostatic mechanism using a thin film and the piezoelectric mechanism the voltage will, for very thin films, be limited by the breakdown field strength. In this case scaling factors for constant field strength are more relevant than pure geometrical scaling factors. In the magnetic mechanism, the scaling factor is given for constant current and for constant current density. To obtain a realistic scaling factor for the electrothermal mechanism, the dissipated power per unit area should be kept constant (as for the optothermal mechanism, where the structure is irradiated by constant radiant intensity). After some manipulations, the same scaling factor as for the optothermal mechanism is obtained.

Table 5.2: Static modal forces and scaling factors of the excitation mechanisms

mechanism	electrode shape $w(x)$	static modal force P_1 [N]	scaling factor
electrostatic (air gap)	$w_{\max} \frac{v_1(x)}{1.59}$	$0.315 \epsilon_0 \frac{w_{\max} l}{d^2} u_0^2 \quad (u_0 \ll u_{\text{pull-in}})$	0 ($u_0 = \text{const}$) 2 ($u_0/u_{\text{pull-in}} = \text{const}$)
electrostatic (thin film)	$\frac{w_{\max}}{0.144l^2} \iint v_1(x) dx dx$	$1.74 \epsilon_{22} \frac{1}{1-\nu} \frac{h_b}{h} \frac{w_{\max}}{l} u_0^2$	0 ($u_0 = \text{const}$) 2 ($u_0/h = \text{const}$)
piezoelectric	$\frac{w_{\max}}{0.144l^2} \iint v_1(x) dx dx$	$3.48 \frac{d_{31}^*}{S_{11}^*} \frac{h_b w_{\max}}{l} u_0$	1 ($u_0 = \text{const}$) 2 ($u_0/h = \text{const}$)
magnetic	not relevant	$-0.831 Bi_0 l$	1 ($i_0 = \text{const}$) 3 ($i_0/(w_b h_b) = \text{const}$)
electro-thermal	$\frac{w_{\max} l^2 (C_1 - 0.0543)}{\left(\iint v_1(x) dx dx + C_1 l^2 \right)}$	$\frac{1}{C_1 - 0.0543} \Gamma_1(\gamma) \frac{E_b h_b^3}{l w_{\max} h} \frac{r \alpha}{k_t} i_0^2$	2 (constant heat per unit area)
optothermal	$\frac{w_{\max}}{0.144l^2} \iint v_1(x) dx dx$	$-6.96 \Gamma_2(\gamma, \xi) \frac{E_b h_b^2 w_{\max}}{l} \frac{\alpha}{k_t} I_0$	2 ($I_0 = \text{const}$)

Other conclusions with respect to the generated modal forces are that the film thickness of the electrostatic mechanism with a thin film should be as small as possible, whereas in the piezoelectric mechanism the film thickness has no effect on the modal force. Absolute comparison of the forces reveals some useful results. The electrostatic mechanism with a thin film produces larger forces than the electrostatic mechanism with an air gap if $(h_b d^2)/(h l^2) > \epsilon_0/\epsilon_{22}$, and larger forces than the piezoelectric mechanism for a field strength $u_0/h > d_{31}^*/(S_{11}^* \epsilon_{22})$. Both conditions are very unlikely to occur; thus it can be concluded that the electrostatic mechanisms with a thin film is a weak mechanism. The ratio of the forces generated by the piezoelectric and the electrostatic mechanism with an air gap equals:

$$\frac{P_{\text{piezoelect}}}{P_{\text{electrost}}} \approx 11 \frac{d_{31}^*}{S_{11}^* \epsilon_0} \frac{1}{u_0} \frac{d^2 h_b}{l^2} \quad (5.20)$$

Only electrostatic resonators realized by very recent technological developments [5.42], [5.43], [5.44], i.e. high aspect ratio air gaps ($l/d \approx 1000$) and very thin beams ($h_b \approx 1 \mu\text{m}$) can compete with piezoelectric resonators (with ZnO active films, i.e. $d_{31} = -5.1 \cdot 10^{-12} \text{ m/V}$, $S_{11} = 7.9 \cdot 10^{-12} \text{ m}^2/\text{N}$ [5.45]) at reasonable voltages (say 1 V). In this sense, we can say that a technological turnover point in favour of electrostatic resonators has just been passed.

5.II.3 The detection mechanisms

Analogue to the excitation mechanisms, we can calculate the magnitude of the electric signals generated by the motion of the resonator. Again this is done for a configuration with one transducer element and one mode. In order to determine the efficiency of the detection mechanism, the resonator is assumed to vibrate with a prescribed amplitude \bar{y}_1 . Only the reversible mechanisms will be considered here. The way in which the electric port is loaded is essential for the magnitude of the output signal.

Possible detection schemes are measuring the voltage at open output ($Z_{load}=\infty$) or measuring the current at short-circuited output ($Z_{load}=0$). The resulting detection signals are given in table 5.3. The shape of the electrode was assumed such that only the first mode of vibration is detected (see second column of the table).

However, from noise considerations, the above load impedances are not a good choice. Optimum signal to noise ratio can be obtained by choosing the load impedance such that maximum power will be dissipated in the load (characteristic load). The average dissipated power in the load impedance can be expressed in the matrix coefficients of the constituent equation:

$$P_{diss} = \frac{|C_{11}|^2}{2|1 + E_{11}/Z_{load}|^2} |\bar{y}_1|^2 \operatorname{Re}(1/Z_{load}) \quad (5.21)$$

If the transducer contains exclusively energy-storing elements, it can be shown that this function has a maximum for $Z_{load}=|E_{11}|$, thus Z_{load} should have a pure resistive character. The corresponding dissipated power equals:

$$P_{diss,max} = \frac{1}{4} \frac{|C_{11}|^2}{|E_{11}|} |\bar{y}_1|^2 \quad (5.22)$$

Expressions for the maximum dissipated power can be obtained by means of the constituent equations (see chapter 5.I). These expressions, as well as the corresponding optimum load resistances are listed in table 5.4. Again, the shape of the detection elements has been taken such that only the first mode is detected, see table 5.1.

If the air gap mechanism and the piezoelectric mechanism (in our opinion the two most prospective mechanisms) are compared, we find the following ratio for the maximum dissipated power:

$$\frac{P_{max,diss,electrost}}{P_{max,diss,piezoel}} \approx \frac{1 - k_{31}^{*2}}{k_{31}^{*2}} \left(\frac{u_0}{u_{pullin}} \right)^2 E_b s_{11}^* \frac{h_b}{h} \quad (5.23)$$

In deriving this result, a relation for the pull-in voltage (eq. (5.28)) has been used, where K_1 is given by eq. (3.20;c) and the first resonance frequency of an unstrained microbridge (eq. (5.30) has been substituted for ω_1). The result allows a straightforward comparison: the ratio of the thickness of film and beam has the same meaning to a piezoelectric resonator as the squared ratio of the bias voltage and the pull-in voltage has to the electrostatically operated resonator. With $k_{31} \approx 0.18$ [5.45] (i.e. $k_{31}^* \approx 0.26$) we see that for the electrostatic mechanism to compete with the piezoelectric mechanism with a ratio $h_b/h=100$, it should be operated at 2.7% of the pull-in voltage. Similar comparisons can be performed for the other mechanisms.

Table 5.3: Current at short circuited output and voltage at open output

mechanism	$w(x)$ [m]	\bar{i} at $Z_{load}=0$ [A]	\bar{u} at $Z_{load}=\infty$ [V]
electrostatic (air gap)	$w_{max} \frac{v_1(x)}{1.59}$	$\bar{i} = -j\omega u_0 \frac{\epsilon_0 w_{max} l}{d^2} \bar{y}_1$	$\bar{u} = 1.20 \frac{u_0}{d} \bar{y}_1$
electrostatic (thin film)	$w_{max} \frac{l^2}{72.0} \left(v_1''(x) + \frac{27.2}{l^2} \right)$	$\bar{i} = -j\omega 3.48 u_0 \frac{h_b}{h} \frac{1}{1-\nu} \epsilon_{22} \frac{w_{max}}{l} \bar{y}_1$	$\bar{u} = 9.20 u_0 \frac{h_b}{l^2} \frac{1}{1-\nu} \bar{y}_1$
piezoelectric	$w_{max} \frac{l^2}{72.0} \left(v_1''(x) + \frac{27.2}{l^2} \right)$	$\bar{i} = j\omega 3.48 \frac{h_b w_{max}}{l} \frac{d_{31}^*}{S_{11}^*} \bar{y}_1$	$\bar{u} = 9.20 \frac{h h_b}{l^2} \frac{k_{31}^{*2}}{d_{31}^* (1 - k_{31}^{*2})} \bar{y}_1$
magnetic	not relevant	$\bar{i} = 0.831 \frac{Bl}{L} \bar{y}_1$	$\bar{u} = j\omega 0.831 B l \bar{y}_1$
piezoresistive	$w(x) < w_b: w(x) \propto 1/\sqrt{\frac{d^2 v_1(x)}{dx^2}}$ $w(x) > w_b: w(x) = w_b$ (see table 3.1)	$\bar{i} = \begin{cases} u_0 / Gr_0 \frac{h_b}{2h} \int_0^l \frac{v_1''(x)}{w(x)} dx \bar{y}_1 & \text{at constant current } i_0 \\ \text{at constant voltage } u_0 & \end{cases}$	$\bar{u} = i_0 Gr_0 \frac{h_b}{2h} \int_0^l \frac{v_1''(x)}{w(x)} dx \bar{y}_1$ at constant current i_0

Table 5.4: Characteristic electric load, maximum dissipated power and scaling of the detection mechanisms

mechanism	$Z_{load\ characteristic}$ [Ω]	$P_{max\ diss}$ [W]	scaling factor
electrostatic (air gap)	$\frac{1.91d}{\epsilon_0 l w_{max} \omega}$	$0.0944 u_0^2 \epsilon_0 \frac{w_{max} l}{d^3} \omega \bar{y}_1^2$	0 ($u_0 = \text{cst}$) 2 ($u_0 / u_{null-in} = \text{cst}$)
electrostatic (thin film)	$\frac{2.65h}{\omega \epsilon_{22} l w_{max}}$	$4.00 u_0^2 \epsilon_{22} \frac{w_{max} h_b^2}{l^3 h} \frac{1}{(1-\nu)^2} \omega \bar{y}_1^2$	0 ($u_0 = \text{cst}$) 2 ($u_0 / h = \text{cst}$)
piezoelectric	$\frac{2.65h}{\epsilon_{33} \omega w_{max} l (1 - k_{31}^{*2})}$	$4.00 \frac{h_b^2 h w_{max}}{l^3} \frac{k_{31}^{*2}}{1 - k_{31}^{*2}} \frac{1}{S_{11}^*} \omega \bar{y}_1^2$	2
magnetic	ωL	$0.0863 \frac{B^2}{L} l^2 \omega \bar{y}_1^2$	3

Again, scaling factors can be derived. They are listed in the right column of table 5.4. In deriving the scaling factors, the amplitude of vibration has also been scaled (it is kept in a constant proportion to the beam dimensions). Further, the fact that the resonance frequency scales as h/l^2 has been used. Again, different scaling factors are derived for some mechanisms

(u_0 is constant, constant field strength, etc.). Just as for the excitation mechanisms, the magnetic mechanism scales least favourable. Further elaboration of this subject is omitted here.

5.II.4 Coupling factors

In the previous section, the electromechanical coupling factor k was introduced. It appears to be a very important characteristic of the system: it is an indication for the quality of the electromechanical transduction. In general, a coupling factor can be defined for any combination of two energy-ports of a system. It is a measure for the fraction of the energy that is offered at one port and can be given to the other one in one cycle. Since we consider only one mode and one transducer, it is an indication for the part of the energy offered at the electrical port that is coupled to the first mode (and vice versa). The coupling factor is defined by:

$$k^2 = C_{11}^{-2}/M_{11}E_{11} \quad (5.24)$$

(for the meaning of C , M and E see eq. (5.1))

General expressions of the coupling factors of the four reversible mechanisms are listed in table 5.5. The coupling factors all have the form $k^2=1/(1+c)$. Apart from the electrostatic mechanism with an air-gap, the coupling factors will generally be much smaller than unity, such that a good approximation is $k^2=1/c$. The coupling factors obtained in this way are also listed in

Table 5.5: Coupling factors of the four reversible mechanisms

mechanism	k^2 [-] (general case)	k^2 [-] (mode 1, $k \ll 1$) see fig. 5.8.
electrostatic (air gap)	$\frac{1}{1 + \frac{C_0}{(\partial C_0 / \partial y_1)^2} \left(\frac{K_1}{u_o^2} - \frac{1}{2} \frac{\partial^2 C_0}{\partial y_1^2} \right)}$	
electrostatic (thin film)	$\frac{1}{1 + 4 \frac{K_1 h A_1 (1 - v^2)}{h_b^2 u_o^2 \epsilon_{22} W_{11}^2} - \frac{v W_{111}^* A_1}{W_{11}^2}}$	$\frac{32.0}{(1-v)^2} \frac{\epsilon_{22} u_o^2}{K_1} \frac{h_b^2 w_{\max}^2}{h l^2}$
piezoelectric	$\frac{1}{1 + 4 \frac{K_1 A_1 s_{11}^* (1 - k_{31}^{*2})}{h_b^2 h W_{11}^2 k_{31}^{*2}}}$	$\frac{32.0}{s_{11}^* K_1} \frac{k_{31}^{*2}}{1 - k_{31}^{*2}} \frac{h_b^2 h w_{\max}}{l^3}$
magnetic	$\frac{1}{1 + \frac{K_1 L}{B^2 V_1^2}}$	$0.690 \frac{B^2 l^2}{K_1 L}$

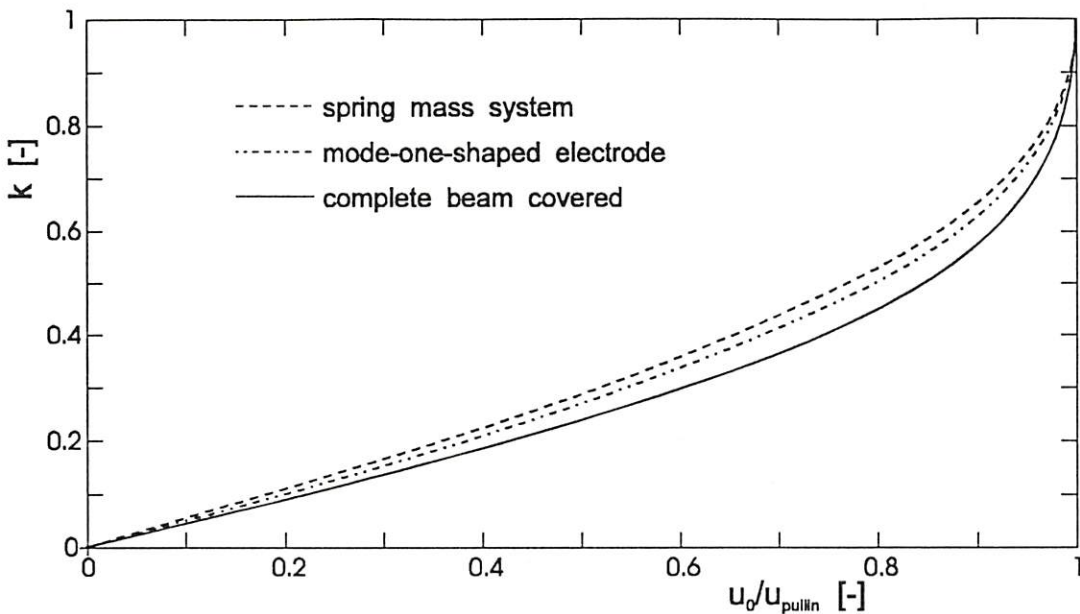


Fig. 5.9: Coupling factor of the electrostatic mechanisms using an air gap as a function of the normalized bias voltage for two different electrode configurations and for a mass-spring system with concentrated elements.

table 5.5. In obtaining the results, the single mode detection patterns as listed in table 5.1 were used. A different electrode geometry just changes the numerical constants.

The coupling factor of the electrostatic mechanism with an air gap cannot be calculated analytically. Numerically obtained values for the coupling factor as a function of the normalized bias voltage are shown in fig. 5.9. The coupling factor increases from 0 to 1 as the bias voltage increases from 0 to the pull-in voltage.

The expression for the coupling factor of the electrostatic mechanism with a thin film can be simplified somewhat by substitution of the spring constant K_1 (eq. (3.20;c)), where the angular resonance frequency ω_r can be written explicitly using eq. (5.30). For the coupling factor, we finally find:

$$k^2 = 0.767 u_0^2 \epsilon_{22} \frac{1}{(1-\nu)^2} \frac{\rho}{E_b} \frac{l w_{\max}^2}{h h_b w_b} \quad (5.25)$$

The coupling factor can be increased by using a high bias voltage. However, for beams of silicon-like materials with silicon-like films and typical aspect ratios ($w_{\max} \approx w_b$, $l/h_b \approx 100$, $w_{\max}/h \approx 10000$) the coupling factor still equals only $k \approx 10^{-6} u_0/\text{Volt}$. The coupling factor is insensitive to proportional scaling of the device. Relative large coupling factors are obtained for wide, thin beams covered with thin dielectric films.

The same simplification can be applied to the piezoelectrically operated resonator. The result is very elegant and reads:

$$k^2 = 0.767 \frac{k_{31}^{*2}}{1 - k_{31}^{*2}} \frac{h}{h_b} \frac{w_{\max}}{w_b} \frac{1}{s_{11}^* E_b} \quad (5.26)$$

The compliance s_{11}^* is just the reciprocal Young's modulus of the film material, such that $s_{11}^* E_b \approx 1$. Further, $w_{\max} \approx w_b$ and $k_{31}^{*2} \ll 1$, such that the squared coupling factor of the system approximately equals the squared intrinsic coupling factor of the film material, k_{31}^* , multiplied

with the thickness ratio of the film and the beam. Hence, this ratio is a very important design parameter. To obtain large coupling factors, h/h_b should be taken large. However, it should not be taken too large since in that case the presence of the film affects the excellent mechanical properties of the crystalline silicon vibrating structure.

5.II.5 Stability

In the previous section, it was shown that the coupling factor of the air gap mechanism equals 1 if the bias voltage equals the pull-in voltage. When the bias voltage approaches the pull-in voltage, the system becomes unstable, and the beam collapses to the fixed plate. From the mechanism treated in this chapter, the air gap mechanism is the only mechanism which shows this type of instability. For a situation with one mode and one electric terminal the conditions for pull-in are: $P_1 = 0$ and $\partial P_1 / \partial y_1 = 0$. The latter condition corresponds to $k=1$. These conditions can be worked out to arrive at the following condition for the deflection at pull-in:

$$\hat{y}_1 - \frac{dC(\hat{y}_1) / d\hat{y}_1}{d^2C(\hat{y}_1) / d\hat{y}_1^2} = 0 \quad (5.27)$$

where \hat{y}_1 is the normalized modal coordinate y_1/d . The value of \hat{y}_1 satisfying eq. (5.27) is called $\hat{y}_{1,pullin}$. The pull-in voltage obeys:

$$u_{pullin}^2 = \frac{2K_1d^3}{d^2C(\hat{y}_{1,pullin}) / d\hat{y}_1^2} = c^2 \frac{K_1d^3}{\epsilon_0 A} \quad (5.28)$$

where A is the electrode surface and c a numerical constant depending on the electrode configuration:

$$c^2 = \frac{2\epsilon_0 \int w(x) dx}{d^2C(\hat{y}_{1,pullin}) / d\hat{y}_1^2} \quad (5.29)$$

We have calculated values of c for two electrode configurations, namely for a mode-one-shaped electrode, and for an electrode covering the entire beam. The corresponding beam deflections have also been calculated. The results are shown in table 5.6. For comparison, the results for a mass-spring system with concentrated elements are also listed.

Table 5.6: Proportionality constants of the pull-in voltage and deflections at pull-in

electrode shape	c [-]	$\hat{y}_1 = y_1/d$ [-]
mode-one-shaped electrode	0.424	-0.238
electrode covering entire beam	0.529	-0.251
mass-spring system	0.544 ($=\sqrt{(8/27)}$)	-0.333 ($=-1/3$)

5.II.6 Resonance frequencies

Although it might not seem so, it is very hard to define the resonance frequency of the resonator system. The resonance frequencies could be defined as those frequencies for which the homogeneous differential equation describing the beams motion eq. has a non-trivial

solution ($v(x) \neq 0$). The frequencies found in this way are from now on referred to as the natural frequencies. The fundamental natural frequency of an axially unloaded microbridge equals:

$$\omega_1 = \sqrt{\frac{K_1}{M_1}} \approx 2\pi 1.028 \sqrt{\frac{\hat{E}_b}{\rho} \frac{h_b}{l^2}} \quad (5.30)$$

The natural frequencies of higher modes and beams with different boundary conditions obey the same relation, however with a different numerical constant. The effect of an axial stress can be described by an additional term (see chapter 3). The natural frequency is a rather mathematical quantity. It is related to, but does not always equal the more important oscillation frequency, that is the frequency at which the oscillator (the resonator placed in its environment) oscillates. This environment includes the excitation and detection mechanism, an electric feed back circuit and mechanical damping.



We concentrate on an 'open loop' configuration (i.e. no feed back circuit). In this section, the effects of the excitation and detection mechanism on the resonance frequency will be discussed. The irreversible excitation mechanisms and the modulator-type detection mechanisms will cause no deviations from the natural frequencies (parametric influences such as temperature dependence of Young's modulus, temperature induced stress etc. are not meant here). However for the reversible mechanisms this is different. For these mechanisms, the resonance frequency could be defined as that frequency for which maximum signal at the output occurs, or the frequency for which the output signal has a certain phase shift with respect to the driving signal. The constituent equation can than be used to calculate the frequency which matches the definition of the resonance frequency. Even for relative simple systems with 1 mode and 2 electric terminals the calculations are rather laborious. It is evident that the load and source characteristics of the electric terminals play an essential role. For example, changing the load at the detection port from $Z_{load} = \infty$ to $Z_{load} = 0$ changes the output signal from a deflection-proportional one to a velocity-proportional one (i.e. 90 deg phase shift). Every intermediate phase shift is possible. So if the resonance frequency is defined in connection with the phase of the output signal, a good knowledge of the sensor environment is an absolute necessity.

A related topic, which will be worked out in more detail, is that the resonance frequency depends on the fact whether the resonator is driven by a current source or a voltage source. If the resonance frequency is defined as that frequency for which the amplitude of the (undamped) vibration grows infinite, the following conditions for resonance can be obtained from the constituent equation eq. (4.4):

$$\text{excitation with current source: } 1 + j\omega M_1 / M_{11} = 0 \quad (5.31.a)$$

$$\text{excitation with voltage source: } 1 - k^2 + j\omega M_1 / M_{11} = 0 \quad (5.31.b)$$

where $\bar{P}_1 = -j\omega M_1 \bar{y}_1$ has been substituted for the dynamic load (viscous friction was neglected). Note that in the magnetic mechanism the role of current and voltage is reversed. If it is realized that the matrix element M_{11} is pure imaginary and proportional to $1/\omega$, we find the following relation between the resonance frequency obtained with a voltage- and a current-source:

$$\frac{\omega_{1,\text{current-source}}^2}{\omega_{1,\text{voltage-source}}^2} = \frac{1}{1 - k^2} \quad (5.32)$$

The voltage-source controlled resonance frequency of the piezoelectric mechanism, and the current-source controlled resonance frequency of the magnetic mechanism both equal the natural resonance frequency. This is due to the specific form of their constituent equations (they obey the relation $1-k^2=K_1/\omega M_{11}$).

Both the voltage- and current-source controlled resonance frequencies of the electrostatic mechanism using a thin film deviate from the natural resonance frequency, but the deviations are small since the coupling factor of this mechanism is usually small. In contrast to the piezoelectric and the magnetic mechanism, the resonance frequencies of this mechanism depend on the bias signal.

Special attention deserves the electrostatic mechanism with an air gap. The resonance frequencies have been calculated in dependence of the bias voltage for three cases (mode-one-shaped electrode, whole beam covered and mass-spring system). The results are shown in fig. 5.10. The voltage-source controlled resonance frequency decreases in all cases from ω_1 to 0 as the bias voltage increases from 0 to $u_{\text{pull-in}}$. In practice, most resonators will be operated at relative low bias voltages. The resonance frequency can then be approximated by a parabolic relation:

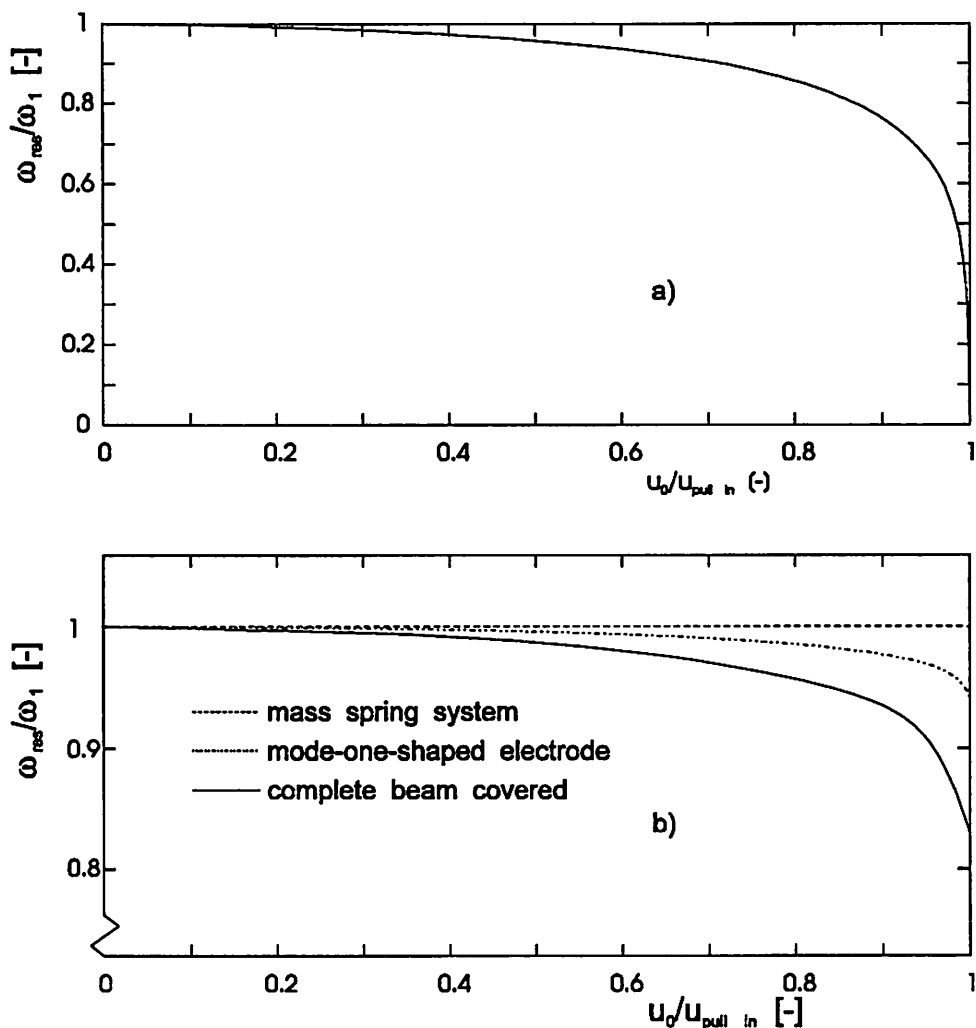


Fig. 5.10: Voltage- (a) and current-source (b) controlled resonance frequency of the air gap mechanism for two different electrode configurations, and for a mass-spring system with concentrated elements.

$$\frac{\omega_{1,voltage\ source}}{\omega_1} \approx 1 - 0.15 \left(\frac{u_0}{u_{pullin}} \right)^2 \quad (k \approx 0.4) \quad (5.33)$$

The current-source controlled resonance frequencies deviate less from the natural frequency. For the mass-spring system, it does not deviate at all. The complicated way in which the resonance frequencies depend on the bias voltage is a severe drawback of this mechanism. It is a direct result from the nonlinear capacity-deflection relation. Devices with a linear capacity-deflection relation (e.g. the laterally resonating electrostatic comb drive devices [5.46]) show a more elegant behaviour. In these devices, the voltage-source controlled resonance frequency simply equals the natural frequency. Other configurations (non resonant) with improved linearity are described in [5.47]. Another advantage of this linear capacitor-deflection devices is that they show no instability. Transversally vibrating resonators with improved linearity could be realized by placing the resonator symmetrically in between two electrodes. Resonators sealed in vacuum microcavities [5.42] and [5.44] are suitable for this purpose, since the sealing cap can be used as the extra electrode.

5.II.7 Conclusions

This chapter concerns a discussion where the model derived in the previous chapter is applied to compare the excitation and detection mechanisms on a variety of aspects. We do not intend to give a decisive answer on the question 'which is the best mechanisms'. Since the mechanisms can be judged on so many aspects, and the choice for a specific mechanism depends very much on the sensor application, technological facilities and other prior conditions, this would be an impossible task. This discussion is mainly meant to provide some useful results which could be of value to those involved in the development of resonant sensors.

Most important conclusions are:

- Most excitation and detection mechanisms are suitable for selective mode operation. Exceptions are the magnetic mechanism and optical detection mechanisms.
- From the reversible mechanisms, the electrostatic mechanism using an air gap and the piezoelectric mechanism produce relatively large excitation forces.
- Excitation forces of the irreversible mechanism can be made very large. A principal limit is the static heating of the resonator. A similar argument holds for the detection signals of the described modulator-type detection mechanism.
- Reversible detection mechanisms are compared assuming an impedance match. Quantitative relations for the maximum obtainable power at the electric port (optimum signal to noise ratio) have been derived for the reversible mechanisms. For the piezoelectric mechanism this power is proportional to the ratio of the thickness of the film and the beam, while for the electrostatic mechanism using an air gap the power is proportional to the squared ratio of the bias voltage and the pull in voltage.
- The magnetic mechanism scales less favourable than the other mechanisms.
- Coupling factors of electrostatic mechanisms depend on the bias voltage. The coupling factor of the electrostatic air gap mechanism can be given any value between 0 and 1. The electrostatic thin film mechanism has very small coupling factors when not using high- ϵ materials. The coupling factor of the piezoelectric mechanism roughly equals the intrinsic

coupling factor of the applied piezoelectric material times the ratio of the thickness of the film and the beam.

- The electrostatic air gap mechanism becomes unstable for too large bias voltages. Simple quantitative relations, assuming bending in the first mode, have been derived for the pull in voltage and deflection at pull in for arbitrarily shaped electrodes.
- When using reversible mechanisms, the resonance frequency (defined on a maximum amplitude of vibration base) depends on the impedance of the driving source. For high impedances (voltage control) the resonance frequency depends on the coupling factor. This in contrast to the case when using low impedances (current control). However, in that case, the resonance frequency can deviate (by a fixed amount) from the resonance frequency of a bare resonator. In the case of the electrostatic air-gap mechanism, the resonance frequency always depends on the bias signal, even when using current control.

PART III:

ELECTRICAL CROSS-TALK IN TWO-PORT RESONATORS -

CASE: THE RESONANT SILICON BEAM FORCE SENSOR¹

5.III.1 Introduction

Resonant silicon sensors, in which the measurand is available as the resonance frequency of a micromechanical structure, offer advantages like high sensitivity, high accuracy and high stability. Furthermore, the output is a frequency, which is less prone to noise and interference and, owing to its semi-digital nature, it is easily combined with digital circuitry [5.48]. Also, the realization process of the sensor structure is based on IC-technology, which makes it possible to add on-chip circuitry, for instance, to realize an electronic oscillator with the sensor as the frequency determining building block.

To excite and to detect the vibrational motion of the micromechanical structure two approaches can be used. One uses a single element, which combines the excitation and detection of the structure and is designated as a one-port resonator [5.49]. The other uses separate elements for excitation and detection of the sensor structure, resulting in a two-port resonator [5.50]. For the excitation and detection several transduction mechanisms are available [5.51].

The performance of (resonant) sensors is degraded by several unwanted effects. In case of a one-port resonator these are due to the parasitic parallel loads, which can obscure the mechanical resonance [5.49]. For a two-port resonator, a similar effect is caused by the electrical cross-talk between the driving port and the detection port [5.52]. The electrical cross-talk is a result of capacitive and/or resistive coupling. In the worst situation, the cross-talk will completely obscure the mechanical resonance of the sensor, making detection of the resonant peak impossible. Also, cross-talk may introduce 'anti-resonance' peaks and/or may induce a shift of the frequency at which the amplitude in the transfer function has a maximum. A proper understanding of the causes of cross-talk is required in order to suppress its degrading influence.

In this paper the electrical cross-talk of two-port resonators is investigated further. A piezoelectrically driven resonant beam force sensor [5.50] is used as an example structure. First, a general model for two-port resonant sensors, including the electrical cross-talk, is discussed using polar diagrams of the different transfer functions. Next, an electrical network, which models the cross-talk of the resonant force sensor, is derived. It is used in conjunction with the mechanical model to simulate the overall sensor transfer function and also to make a comparison with the measured results. Further, the reduction of the cross-talk as a result of changes in the sensor geometry and the sensor configuration is investigated. Measurement results are presented together with simulations.

¹ Based on: C.J. van Mullem, Micromachined silicon integrated resonant sensors, Chapter 3.4, PhD thesis University of Twente, Enschede the Netherlands

5.III.2 Two-port resonator - The transfer function

The overall transfer function $\bar{H}(j\omega)$ of a two-port resonant sensor can be written as the sum of two contributions: $\bar{M}(j\omega)$, representing the mechanical behavior and $\bar{E}(j\omega)$, representing the electrical cross-talk. This is shown schematically in Fig. 5.11.

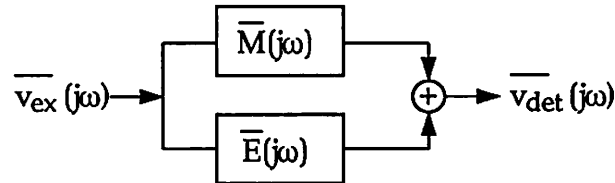


Fig. 5.11 Block diagram of the overall transfer function of a two-port resonant sensor: $\bar{H}(j\omega) \equiv \bar{v}_{det}(j\omega)/\bar{v}_{ex}(j\omega) = \bar{M}(j\omega) + \bar{E}(j\omega)$, where $M(j\omega)$ represents the mechanical behavior and $E(j\omega)$ represents the electrical cross-talk. Noise is ignored in this diagram.

In phasor notation the transfer function can be expressed as:

$$\bar{H}(j\omega) = \bar{M}(j\omega) + \bar{E}(j\omega) \quad (5.34)$$

as illustrated in Fig. 5.12. In this figure, the cross-talk $\bar{E}(j\omega)$ is assumed to be constant in a narrow frequency range around the fundamental mode. The mechanical transfer function $\bar{M}(j\omega)$ is approximated by a circle, being characteristic for resonance. The amplitude $|\bar{M}(j\omega)|$ is maximal at a phase angle φ_M of 90° occurring at a frequency $\omega = \omega_1$. The diameter of the circle depends on the electromechanical transduction factor α , as defined by Van Vlerken et al. [5.53], and on the quality factor of the resonator. High quality factors imply large diameter circles.

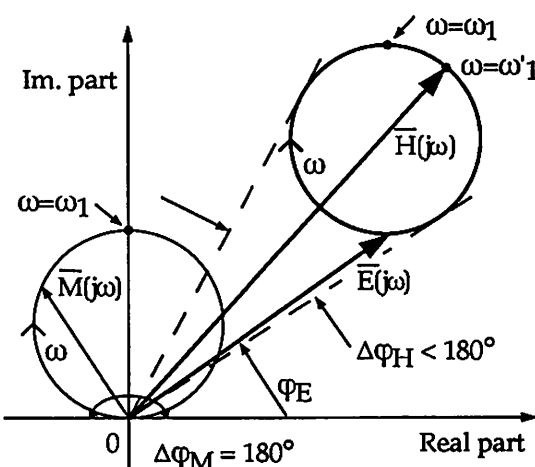


Fig. 5.12 Theoretical polar diagram of the different transfer functions of a two-port resonator (also see Fig. 5.11). $E(j\omega)$ is assumed to be constant in the frequency range around the fundamental mode. Noise is ignored in this diagram.

From eqn. (5.34) expressions for the magnitude $|\bar{H}(j\omega)|$ and phase φ_H can be derived:

$$|\bar{H}(j\omega)| = |\bar{M}(j\omega)| \left[\left(\cos(\varphi_M) + \frac{|\bar{E}(j\omega)|}{|\bar{M}(j\omega)|} \cos(\varphi_E) \right)^2 + \left(\sin(\varphi_M) + \frac{|\bar{E}(j\omega)|}{|\bar{M}(j\omega)|} \sin(\varphi_E) \right)^2 \right]^{\frac{1}{2}} \quad (5.35)$$

$$\varphi_H = \arg \bar{H}(j\omega) = \arctan \left[\frac{\sin(\varphi_M) + \frac{|\bar{E}(j\omega)|}{|\bar{M}(j\omega)|} \sin(\varphi_E)}{\cos(\varphi_M) + \frac{|\bar{E}(j\omega)|}{|\bar{M}(j\omega)|} \cos(\varphi_E)} \right] \quad (5.36)$$

where φ_M and φ_E are the phase angles of the mechanical and electrical transfer function, respectively. In Fig. 5.13 a typical Bode plot of $\bar{H}(j\omega)$ is given. In this figure, as opposed to Fig. 5.12, $\bar{E}(j\omega)$ is now frequency dependent. From eqns. (5.35) and (5.36) it can be seen that for small values of the ratio $|\bar{E}(j\omega)|/|\bar{M}(j\omega)|$ the electrical cross-talk can be ignored and $|\bar{H}(j\omega)|$ and φ_H will approach $|\bar{M}(j\omega)|$ and φ_M , respectively.

The electrical cross-talk introduces an off-set of the resonance loop in the complex plane. This has several consequences. First of all, the frequency at which the amplitudes of $|\bar{M}(j\omega)|$ and $|\bar{H}(j\omega)|$ are maximal are no longer the same. For the example shown in Fig. 5.12, the maximum of $|\bar{H}(j\omega)|$ occurs at a (slightly) higher frequency, ω'_1 , than the frequency ω_1 ($<\omega'_1$)

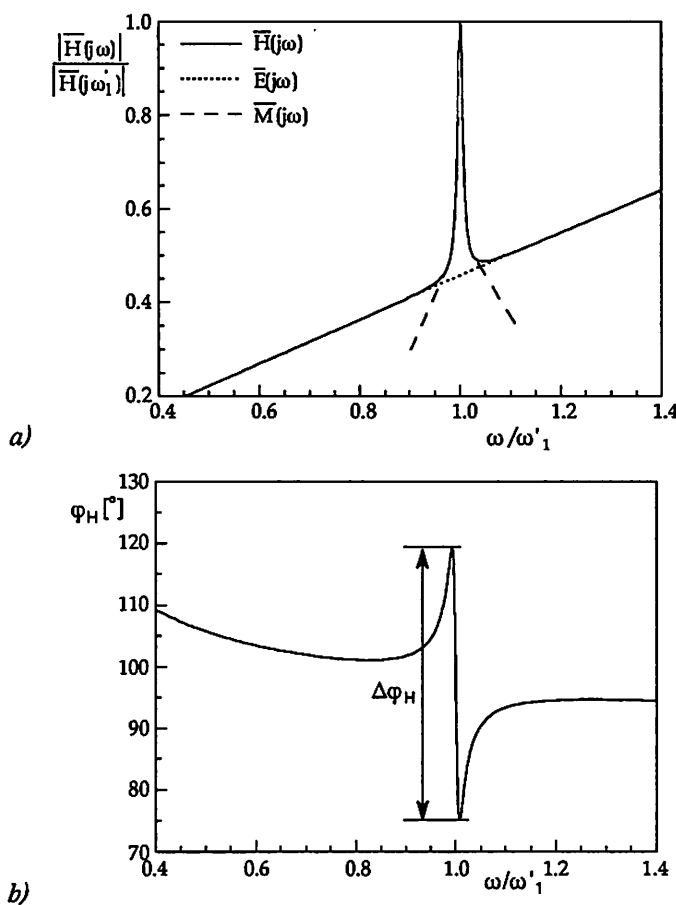


Fig. 5.13 Simulated typical Bode plots. (a) normalized modulus; (b) phase angle. $\Delta\varphi$ is the maximum observed phase shift as indicated in Fig. 5.12.

at which $\bar{M}(j\omega)$ has its maximum. The relative change in magnitude also becomes smaller due to the cross-talk. Furthermore, the expected phase shift $\Delta\varphi$ of 180° in the frequency interval around resonance will be smaller (see Fig. 5.13). All this makes the mechanical resonance less pronounced, calling for compensation and/or reduction of the cross-talk.

Two approaches can be used to minimize the electrical cross-talk. First, a compensation technique can be chosen. An example is an on-chip differential electrical design where another identical electrical structure is realized in addition to the sensor structure. Here, the total output signal is given by the sensor output minus the output of the electrical structure in order to eliminate the electrical cross-talk. Secondly, the sensor structure and/or the sensor geometry can be optimized. This solution will be described further in the next paragraph.

5.III.3 The resonant silicon beam force sensor [5.50]

The structure

A schematic drawing of the sensor is shown in Fig. 5.14. The heart of the sensor is a silicon beam. Piezoelectric layers of ZnO are used for the excitation and detection of the vibration. A double layer of ZnO and SiO₂ is sandwiched between a p⁺⁺-bottom and an aluminum top electrode. The SiO₂ is used to insulate the top from the bottom electrode and forms, in combination with the ZnO layer, a dielectric medium for the piezoelectric excitation and detection [5.54,5.55].

Theoretical model of the electrical and mechanical transfer function

The model for the electrical transfer function of the resonant force sensor is based on the cross-section of Fig. 5.14. An equivalent electrical lumped element network of the sensor is shown in Fig. 5.15. The bottom electrode is modelled with five resistors (R_{1-5}). The SiO₂ and the ZnO layers are modelled as a parallel combination of a capacitor (C_{SiO_2} and C_{ZnO}) and a resistor (R_{SiO_2} and R_{ZnO}). The model assumes that the ZnO layer is completely depleted [5.55]. The input capacitor (C_i) represents the capacitance between the top and the bottom electrode and R_i the d.c. resistance of the SiO₂ layer sandwiched between the aluminum and the p⁺⁺-layer. In the model the parasitic impedances caused by wires, probes and housing are not taken into account.

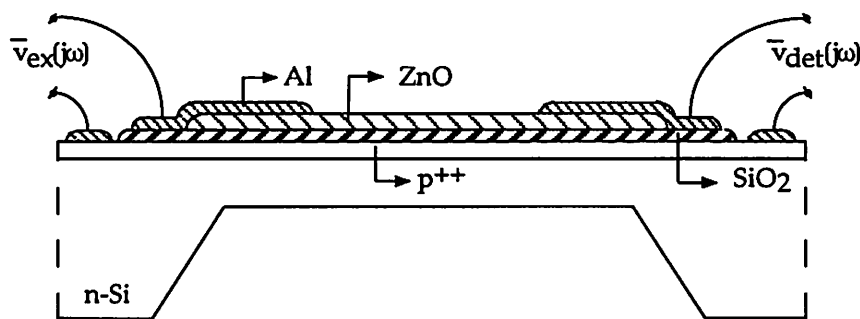


Fig. 5.14 Cross-sectional diagram of the resonant silicon beam force sensor [5.50]. Beam dimensions: length = 6mm, width = 0.4mm and thickness = 20μm.

The origin of the electrical cross-talk can be explained with the circuit of Fig. 5.15. An input voltage will produce an output voltage because of the electrical connection between the input port and the output port. The finite resistivity of the bottom electrode means that node A is not at ground potential. Theoretically, if node A is grounded the cross-talk will be completely suppressed.

The mechanical transfer function $\bar{M}(j\omega)$ of the resonant force sensor is modelled by a lumped element model [5.50] as shown in Fig. 5.15 and applies for a narrow frequency range around the fundamental vibrational mode. With ideal transformers the electrical input is converted into the mechanical domain, where each vibrational mode (n) is represented by a modal mass $L_{m,n}$, a compliance $C_{m,n}$ and a resistance $R_{m,n}$, and back into the electrical domain. The model can easily be extended to include other modes. The piezoelectric transduction is reflected in the transformer turn ratio a . The efficiency of the transduction is decreased since only a fraction of the input voltage will appear across the ZnO layer. This fraction can be increased if the ZnO layer is deposited directly on top of the p⁺⁺-bottom electrode [5.55]; this way the voltage drop across the oxide layer is avoided.

Measured and simulated overall transfer function

In Fig. 5.16 a measured and simulated polar plot of $\bar{H}(j\omega)$ is given. Both plots clearly indicate that $\bar{H}(j\omega)$ is equal to the sum of the two transfer functions $\bar{M}(j\omega)$ and $\bar{E}(j\omega)$, (compare Fig. 5.12). The electromechanical transduction factor α is adjusted in order to obtain the same loop diameter for the simulated plot as for the measured plot. The measured $\Delta\phi_H$ is about 40° and the maximum $|\bar{H}(j\omega_1)|$ is -75dB. The unloaded resonance frequency f_1 is around 4.8 kHz which is close to the theoretical value of 4.9kHz.

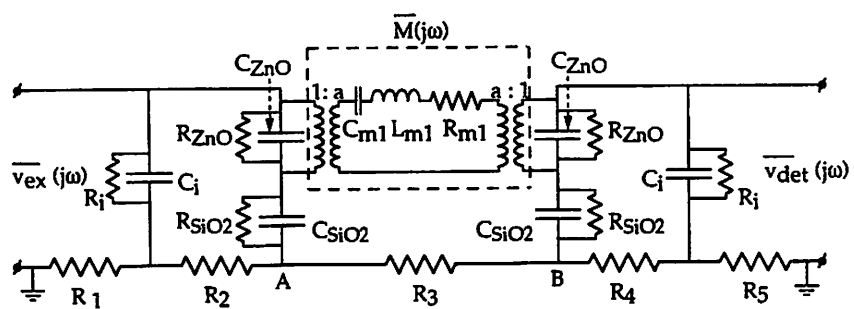


Fig. 5.15 Equivalent electrical network of the resonant beam force sensor for a floating substrate. C_{m1} and L_{m1} are functions of the specific mass and the beam dimensions and R_{m1} represents the energy losses [5.53]. The model is valid for a narrow frequency range around the fundamental frequency ω_1 . The transformer couples energy from the electrical domain to the mechanical domain and vice versa. The transformer turn ratio a depends on the electromechanical transduction factor α and on the mode shape [5.50].

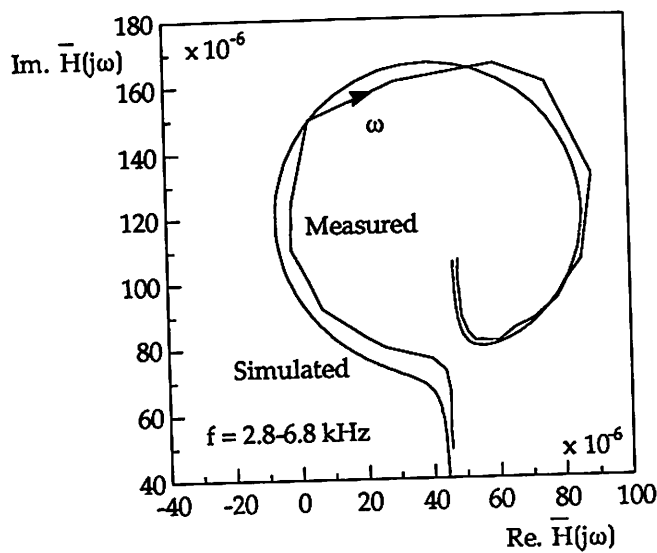


Fig. 5.16 Measured and simulated polar diagram of $\bar{H}(j\omega)$ of the sensor shown in Fig. 5.14.

Reduction of the electrical cross-talk

To reduce the influence of $\bar{E}(j\omega)$ on $\bar{H}(j\omega)$ the sensor structure itself is investigated. Looking at the equivalent network for the electrical cross-talk in Fig. 5.15, reduction can be achieved by:

- reducing the series resistance from point A and/or B to ground;
- reducing the capacitances to decrease the voltage on node A (B);
- increasing the impedance between points A and B;
- low leakage dielectric layers to increase the d.c. parallel resistance.

Implementation of the above is possible by the following means.

(1) *The use of other materials.* For example, a metal can be used instead of a p^{++} -layer for the bottom electrode in order to lower the resistivity of the bottom electrode. This way, node A will be grounded. A disadvantage, however, is the lack of stress compensation, since the tensile stress in the p^{++} -bottom electrode is used to compensate the compressive stress of the ZnO layer [5.50]. Also, materials can be chosen which have a higher d.c. resistance than CVD oxide, for example, thermal oxide or LPCVD silicon nitride.

(2) *The change of the sensor geometry.* The value of relevant components in the geometry can be changed to reduce the voltage at node A. These components are the capacitor C_i and the resistors R_1 and R_5 . The other components (C_{ZnO} , C_{SiO_2} and R_{2-4}) are dictated by the required mechanical characteristics, making adjustments less flexible. The modified geometry will have a smaller bonding pad area and, furthermore, the aluminum contact for the bottom electrode is moved closer to the end of the sensor beam.

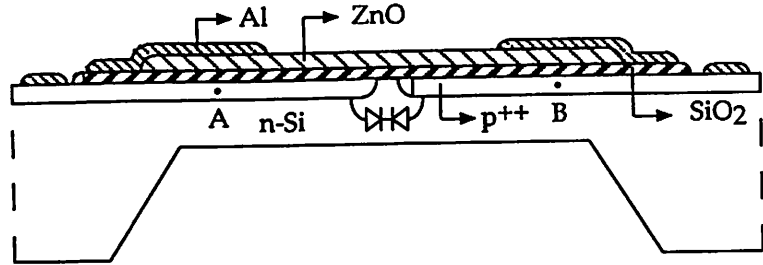


Fig. 5.17 Cross-sectional diagram of the resonant silicon beam force sensor with interrupted bottom electrode by means of two anti-serial pn-junctions

(3) *The change of the sensor configuration.* Interrupting the bottom electrode by means of two anti-serial pn-junctions will increase R_3 and thus provides a high-resistance path between points A and B (see Fig. 5.17). The sensor is realized in an n-type silicon wafer. As indicated before, the tensile stress in the p⁺⁺-layer compensates the compressive stress in the ZnO layer. For a small interruption (20 μm) stress compensation is still accomplished.

Solutions (2) and (3) have actually been realized and the measured results are shown in Fig. 5.18. Interruption of the bottom electrode gives a stronger reduction of the cross-talk. The modified geometry and interruption of the bottom electrode result in a cross-talk level of the order of the noise level for the frequency range of interest, that is, 1-30kHz. The second solution has also been simulated including the mechanical model. The results are shown in Fig. 5.19. It is clearly seen that the level of cross-talk is reduced which will move the resonance loop closer to the origin. The cross-talk still effects the phase shift but the overall phase shift approaches 180°. An additional improvement is the increase of the diameter of the circle. The change of the geometry increases the fraction of the input voltage which appears across the ZnO capacitor. Both the decrease of the cross-talk and the larger diameter imply an increase in the relative change of magnitude.

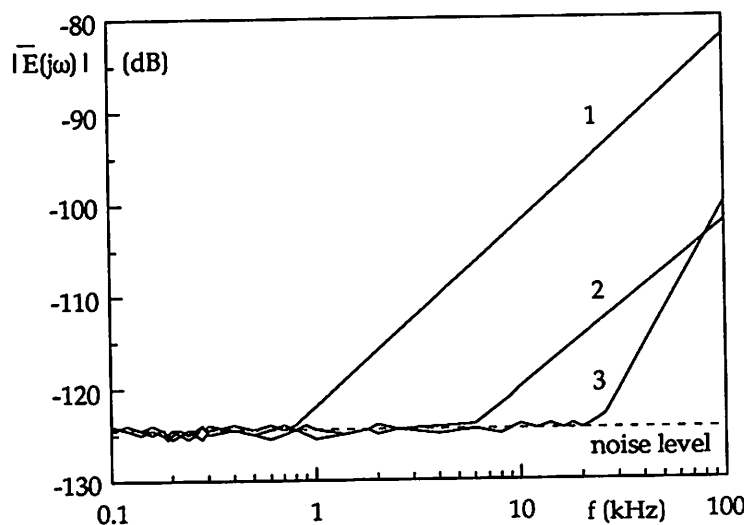


Fig. 5.18 Measured and simulated electrical transfer function, (1) original design, (2) after adjusting C_1 , R_1 and R_5 , (3) after interrupting the bottom electrode.

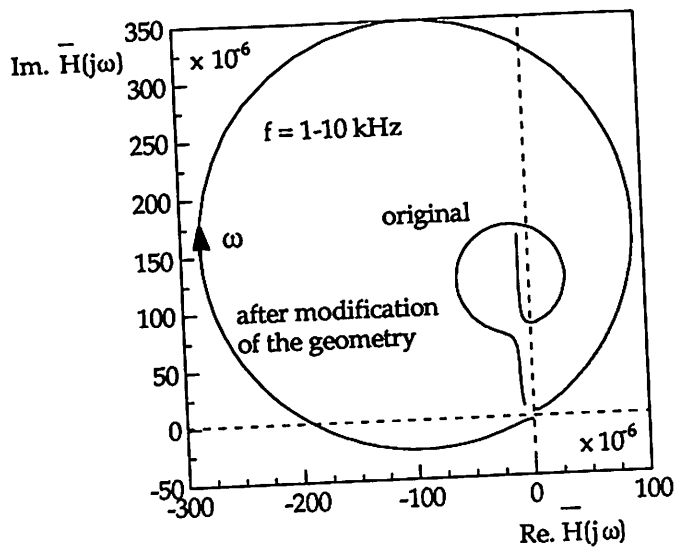


Fig. 5.19 Simulated overall sensor transfer function for two different levels of cross-talk.

5.III.4 Conclusions

Besides the mechanical coupling, $\bar{M}(j\omega)$, between the input and output port of two-port resonant sensors, an electrical coupling, $\bar{E}(j\omega)$, due to cross-talk, exists. The cross-talk is caused by capacitive and/or resistive coupling between the driving port and detection port of the sensor. The overall transfer function $\bar{H}(j\omega)$ can be written as the vectorial sum of $\bar{M}(j\omega)$ and $\bar{E}(j\omega)$. In a polar diagram, $\bar{H}(j\omega)$ is shifted away from the origin due to the electrical component. In a Bode plot, $\bar{E}(j\omega)$ manifests itself as a decrease of the maximum phase shift of $\bar{H}(j\omega)$ around resonance and, further, by a decrease of the relative change in magnitude. Both effects will make the detection of the mechanical resonance more difficult.

The resonant silicon beam force sensor with piezoelectric excitation and detection of the vibrational motion of the beam has been analyzed. In the original design, the electrical cross-talk limited the maximum phase shift to about 40° . To reduce the cross-talk level and to increase the phase shift of $\bar{H}(j\omega)$ two solutions were investigated. First, the value of relevant components in the sensor geometry were changed. Second, the bottom electrode was interrupted by means of two anti-serial pn-junctions. Applying both at the same time results in a cross-talk level close to the noise level for the frequency range of interest. Also, the overall phase shift approaches the 180° due to the reduction of the electrical cross-talk.

References

- [5.1] G. Stemme, *Resonant silicon sensors*, J. Micromech. Microeng., 1 (1991), 113-125.
- [5.2] H.A.C. Tilmans, M. Elwenspoek and J.H.J. Fluitman, *Micro resonant force gauges*, Sensors and Actuators A, 30 (1992), 35-53.
- [5.3] M. Elwenspoek, F.R. Blom, S. Bouwstra, T.S.J. Lammerink, F.C.M. van de Pol, H.A.C. Tilmans, Th.J.A. Popma and J.H.J. Fluitman, *Transduction mechanisms and their application in micromechanical devices*, Proc. Micro Electro Mechanical Systems (MEMS 89), Salt Lake City, UT, USA, Feb. 1989, 126-132.
- [5.4] M. Dufour, M.T. Delaye, F. Michel, J.S. Danel, B. Diem and G. Delapierre, *A comparison between micromachined pressure sensors using quartz or silicon vibrating beams*, Proc. 6 th Int. Conf. Solid-State Sensors and Actuators (Transducers '91), San Fransisco, CA, USA, 24-27 June 1991, 668-671.
- [5.5] P.E. Wellstead, *Introduction to physical system modelling*, Academic Press, London, 1979.
- [5.6] D. Karnopp and R. Rosenberg, *System dynamics: a unified approach*, John Wiley & Sons, New York, 1975.
- [5.7] R.T. Howe and R.S. Muller, *Resonant-microbridge vapor sensor*, IEEE Trans. Electron Devices, ED-33 (1986), 499-506.
- [5.8] H.C. Nathanson, W.E. Newell, R.A. Wickstrom and J. Ransford Davis, Jr., *The Resonant Gate Transistor*, IEEE Trans. Electron Dev., ED-14 (1967), 117-133.
- [5.9] E. Stemme and G. Stemme, *A capacitively excited and detected resonant pressure sensor with temperature compensation*, Sensors and Actuators A, 32 (1992), 639-647.
- [5.10] J.C. Greenwood, *Etched Silicon Vibrating Sensor*, J. Phys. E: Sci. Instrum., 17 (1984), 650-652.
- [5.11] M.W. Putty, S.C. Chang, R.T. Howe, A.L. Robinson and K.D. Wise, *One-port active polysilicon resonant microstructures*, Proc. Micro Electro Mechanical Systems (MEMS 89), Salt Lake City, UT, USA, Feb. 1989, 60-65.
- [5.12] J.J. Sniegowski, H. Guckel and T.R. Christenson, *Performance characteristics of second generation polysilicon resonating beam force transducers*, Proc. IEEE Solid-State Sensors and Actuators Workshop, Hilton Head Island, SC, USA, 4-7 June 1990, 9-12.
- [5.13] C. Linder, E. Zimmermann and N.F. de Rooij, *Capacitive polysilicon resonator with MOS detection circuit*, Sensors and Actuators A, 25-27 (1991), 591-595.
- [5.14] K. Petersen, F. Pourahmadi, J. Brown, P. Parsons, M. Skinner and J. Tudor, *Resonant silicon beam pressure sensor fabricated with silicon fusion bonding*, Proc. 6 th Int. Conf. Solid-State Sensors and Actuators (Transducers '91), San Fransisco, CA, USA, 24-27 June 1991, 664-667.
- [5.15] S. Bouwstra, F.R. Blom, T.S.J. Lammerink, H. Yntema, P. Schrap, J.H.J. Fluitman and M. Elwenspoek, *Excitation and detection of vibrations of micromechanical structures using a dielectric thin film*, Sensors and Actuators, 17 (1989), 219-223.
- [5.16] T.S.J. Lammerink, M. Elwenspoek and J.H.J. Fluitman, *Thermal actuation of clamped silicon microbeams*, Sensors and Materials, 3 (1992), 217-238.
- [5.17] A. Prak, M. Elwenspoek and J.H.J. Fluitman, *Selective mode excitation and detection of micromachined resonators*, Proc. Micro Electro Mechanical Systems (MEMS 92), Travemünde, Germany, Feb. 1992, 220-225.
- [5.18] C.J. van Mullem, F.R. Blom, J.H.J. Fluitman and M. Elwenspoek, *Piezoelectrically driven silicon beam force sensor*, Sensors and Actuators A, 25-27 (1991), 379-383.
- [5.19] J. Soderkvist, *Activation and detection of mechanical vibrations in piezoelectric beams*, Sensors and Actuators A, 32 (1992), 567-571.
- [5.20] D.A. Berlincourt, D.A. Curran, H. Jaffe, *Piezoelectric and piezomagnetic materials and their function in transducers*, in W.P. Mason (ed), *Physical acoustics*, Vol. 1, Part A, Academic Press, New York, London, 1964.
- [5.21] J.G. Smits, S.I. Dalke and T.K. Cooney, *The constituent equations of piezoelectric bimorphs*, Sensors and Actuators A, 28 (1991), 41-61.
- [5.22] J.G. Smits and W. Choi, *The constituent equations of piezoelectric heterogeneous bimorphs*, IEEE Trans. Ultrason. Ferroel. Freq. Contr., 38 (1991), 256-270.
- [5.23] K. Ikeda, H. Kuwayama, T. Kobayashi, T. Watanabe, T. Nishikawa, T. Yoshida and K. Harada, *Three-dimensional micromachining of silicon pressure sensor integrating resonant strain gauge on diaphragm*, Sensors and Actuators, A21-A23 (1990), 1007-1010.

- [5.24] K. Hane and S. Hattori, *Photothermal excitation of a layered sample in plate form*, Applied Optics, 29 (1990), 145-150.
- [5.25] D.W. Satchell and J.C. Greenwood, *A thermally excited silicon accelerometer*, Sensors and Actuators 17 (1989), 241-245.
- [5.26] S. Bouwstra, R. Legtenberg, H.A.C. Tilmans and M. Elwenspoek, *Resonating microbridge mass flow sensor*, Sensors and Actuators, A21-A23 (1990), 332-335.
- [5.27] R.J. Wilfinger, P.H. Bardell, D.S. Chhabra, *The resonistor, a frequency selective device utilizing the mechanical resonance of a silicon substrate*, IBM J. Res. Developm., 12 (1968), 113-118.
- [5.28] T.S.J. Lammerink and W. Włodarski, *Integrated thermally excited resonant diaphragm pressure sensor*, Proc. 3rd Int. Conf. Solid-State Sensors and Actuators (Transducers '85), Philadelphia, PA, USA, 11-14 June 1985, 97-100.
- [5.29] D. Moser, O. Brand and H. Baltes, *A CMOS compatible thermally excited silicon oxide beam resonator with aluminium mirror*, Proc. 6 th Int. Conf. Solid-State Sensors and Actuators (Transducers '91), San Francisco, CA, USA, 24-27 June 1991, 547-550.
- [5.30] W. Benecke, A. Heuberger, W. Riethmüller, U. Schnakenberg, H. Wölfelschneider, R. Kist, G. Knoll, S. Ramakrishnan and H. Höfflin, *Optically excited mechanical vibrations in micromachined silicon cantilever beams*, Proc. 4th Int. Conf. Solid-State Sensors and Actuators (Transducers '87), Tokyo, Japan, 2-5 June 1987, 838-842.
- [5.31] K.E.B. Thornton, D. Uttamchandani and B. Culshaw, *A sensitive optically excited resonator pressure sensor*, Sensors and Actuators A, 24 (1990), 15-19.
- [5.32] T. Kvisterøy, O.H. Gusland, B. Stark, H. Nakstad, M. Eriksrud and B. Bjørnstad, *Optically excited silicon sensor for permanently installed downhole pressure monitoring applications*, Sensors and Actuators A, 31 (1992), 164-167.
- [5.33] B.S. Douma and P. Eigenraam, *Modelling the pressure and temperature sensitivity of an optically excited micromachined silicon sensor for permanently installed downhole monitoring systems*, Sensors and Actuators A, 31 (1992), 215-219.
- [5.34] A. Prak and T.S.J. Lammerink, *Effect of electronic strain on the optically induced mechanical moment in silicon micro-structures*, J. Appl. Phys., 71 (1992), 5242-5245. See also section 6.1 of this thesis.
- [5.35] Y. Kanda, *Piezoresistance effect of silicon*, Sensors and Actuators A, 28 (1991), 83-91.
- [5.36] R.A. Buser, N.F. de Rooij and L. Schultheis, *Silicon pressure sensor based on a resonating element*, Sensors and Actuators A, 25-27 (1991), 717-722.
- [5.37] M.V. Andres, M.J. Tudor and K.W.H. Foulds, *Analysis of an interferometric optical fibre detection technique applied to silicon vibrating sensors*, Electr. Lett., 23 (1987), 774-775.
- [5.38] R.M. Langdon and D.L. Dowe, *Photoacoustic oscillator sensors*, SPIE Vol. 798, Fiber Optic Sensors II 1987, 86-93.
- [5.39] T.S.J. Lammerink and S.J. Gerritsen, *Fiber-optic sensors based on resonating mechanical structures*, SPIE Vol. 798, Fiber Optic Sensors II 1987, 67-71.
- [5.40] C.A.J. Putman, B.G. de Groot, N.F. van Hulst and J. Greve, *A detailed analysis of the optical beam deflection technique for use in atomic force microscopy*, J. Appl. Phys., 72 (1992), 6-12.
- [5.41] A. Prak, M. Elwenspoek and J.H.J. Fluitman, *Selective mode excitation and detection of micromachined resonators*, J-MEMS p4 (1992), 179-186.
- [5.42] J.J. Sniegowski, H. Guckel and T.R. Christenson, *Performance characteristics of second generation polysilicon resonating beam force transducers*, Proc. IEEE Solid-State Sensors and Actuators Workshop, Hilton Head Island, SC, USA, 4-7 June 1990, 9-12.
- [5.43] C. Linder, E. Zimmermann and N.F. de Rooij, *Capacitive polysilicon resonator with MOS detection circuit*, Sensors and Actuators A, 25-27 (1991), 591-595.
- [5.44] H.A.C. Tilmans et al., *Mechanical characteristics of electrostatically driven vacuum encapsulated polysilicon resonators*, Submitted to IEEE Ultrason. Ferroel. Freq. Control.
- [5.45] I.B. Kobiakov, *Elastic, Piezoelectric and dielectric properties of ZnO and CdS single crystals in a wide range of temperatures*, Solid State Communications, 35 (1980), 305-310.
- [5.46] W.C. Tang, T.H. Nguyen, M.W. Judy and R.T. Howe, *Electrostatic comb drive of lateral polysilicon resonators*, Sensors and Actuators, A21-A23 (1990), 328-331.
- [5.47] L. Rosengren, J. Söderkvist and L. Smith, *Micromachined sensor structures with linear capacitive response*, Sensors and Actuators A, 31 (1992), 200-205.

- [5.48] S. Middelhoek, P.J. French, J.H. Huijsing and W. J. Lian, Sensors with digital or frequency output, *Sensors and Actuators*, 15 (1988), 119-133.
- [5.49] H.A.C. Tilmans, D.J. IJntema and J.H.J. Fluitman, Single element excitation and detection of (micro-) mechanical resonators, *Proc. 6th Int. Conf. Solid-State Sensors and Actuators (Transducers'91)*, San Francisco, USA, 1991, pp. 533-537.
- [5.50] C.J. van Mullem, F.R. Blom, J.H.J. Fluitman and M. Elwenspoek, Piezoelectrically driven silicon beam force sensor, *Sensors and Actuators A*, 25-27 (1991) 379-383.
- [5.51] M. Elwenspoek, F.R. Blom, S. Bouwstra, T.S.J. Lammerink, F.C.M. van de Pol, H.A.C. Tilmans, Th. J. A. Popma and J.H.J. Fluitman, Transduction mechanisms and their applications in micromechanical devices, *Proc. IEEE Micro Electro Mechanical Systems (MEMS'89)*, Salt Lake City, 1989, pp. 126-132.
- [5.52] R.T. Howe and R.S. Muller, Resonant-microbridge vapor sensor, *IEEE Trans. on Electron Devices*, ED-33 (1986) 499-506.
- [5.53] J.J.L.M. van Vlerken, S. Bouwstra, F.R. Blom, J.H.J. Fluitman, P.C. Breedveld, Finite-mode bond-graph model of a resonant silicon-beam force sensor, *Int. Journal on Modelling and Simulation*, 12 (1991) 44-49.
- [5.54] F.R. Blom, D.J. IJntema, F.C.M. van de Pol, M. Elwenspoek, J.H.J. Fluitman and Th. J. Popma, Thin-film ZnO as micromechanical actuator at low frequencies, *Sensors and Actuators*, A21-A23 (1990) 226-228.
- [5.55] F.R. Blom, F.C.M. van de Pol, G. Bauhuis and Th.J.A. Popma, (R.F. planar magnetron sputtered) ZnO films II: electric properties, *Thin Solid Films*, 204 (1991) 365-376.